

Revisit the Oort constants measurement from *Gaia DR2* observations and simulations

SHUFAN XIA,¹ KARENS MASTERS,¹ AND ZHAO-YU LI²

¹*Haverford College, Department of Physics and Astronomy*

²*Shanghai Jiaotong University, Department of Astronomy*

ABSTRACT

The Oort constants are a set of empirical constants which can be used to reveal rotational kinematics of the Milky Way (MW) disk in the solar neighborhood. The orbital properties of the Sun can be estimated from the Oort constants. They are also used to derive the radial profiles of the circular velocity in the MW and the mass density profile. An accurate determination of this set of constants helps us derive the MW rotation curve in the Sun's immediate neighborhood and to understand the general kinematic properties of the MW disk. *Gaia* provides massive and exquisite data on parallax and proper motion for billions of stars in the Milky Way. These data make it possible to determine the Oort constants in the solar vicinity with unprecedented accuracy. In this thesis, combining test particle simulation and the recent *Gaia* DR2 data, we examine the influence of different sampling criteria of the stellar distance and latitude ranges in Galactic Coordinates in deriving the Oort constant. From the simulation, it seems that it is necessary to limit the distance within 1kpc and latitude range $|b| < 20^\circ$ to achieve a good fit based on the longitudinal profiles of μ_l and v_{los} . The longitudinal profile of μ_b is generally not as good as the other two kinematic tracers. However, reasonable Oort constants could be estimated if the latitude range is limited to $30^\circ < |b| < 50^\circ$. We apply the sample selection criteria from previous literature on using proper motion and line-of-sight velocity data from *Gaia* DR2 and compare the result with the criteria determined from our test particle simulations. We found $A = 15.52 \pm 0.22$, $B = -13.33 \pm 0.17$, $C = -1.88 \pm 0.08$, and $K = -1.86 \pm 0.19$ km/s/kpc from *Gaia* DR2 observational data, consistent with previous works.

1. INTRODUCTION

The simplest model of the Milky Way proposes that our galaxy is a flattened round disk, and stars move on perfectly circular orbits around the Galactic center (GC). However, the structure and the dynamics of our galaxy is much more complicated. Our galaxy is a barred-spiral galaxy with non-axisymmetric and time-dependent potential perturbation. In reality, all stars have non-circular components to their orbital energy, so they move in “rosette” and non-closed orbits (Binney & Merrifield 1998; Bovy 2017). The rotational kinematics of the MW are, therefore, complicated to quantify. The Oort constants are a set of empirically derived kinematic parameters notated typically with A , B , C , and K that characterizes the local rotational properties in the Milky Way. They have been used extensively in the study of the rotational kinematics of our galaxy.

To help us keep track of the different types of velocities in the following discussion, here I list the notation for velocity components used throughout this paper. In Galactocentric cylindrical coordinate, v_{circ} or v_ϕ is the circular velocity about the GC; v_r is the radial velocity with respect to the GC; v_z is vertical velocity away from the MW plane. In Galactic coordinates (discussed further in Section 1.2), v_{los} is the line of sight velocity as seen from the Sun; v_l is the velocity component perpendicular to the line of sight in the Galactic longitude (l) direction; and v_b represents the velocity component perpendicular to the line of sight in the Galactic latitude (b) direction.

1.1. *The Milky Way Rotation Curve*

The rotation curves of galaxies are used to illustrate the variation of circular rotational velocity, v_{circ} , about the Galactic center along different distances from the center. Pioneered by Vera Rubin, galaxy rotation curves have been studied as the evidence of Dark Matters. For our Milky Way, this rotation curve is flat but slightly declining from the radius of the Sun and beyond. The mass components and their distributions in our Galaxy have been derived from this curve. Fig. 1 shows a recent measurement of the MW rotation curve (Eilers et al. 2019). The overall rotation curve comes from adding up the contributions from different components of mass - the central bulge, stellar disc, other stellar components and the dark matter halo (Olling & Merrifield 1998).

Using Newtonian Mechanics, we can connect velocity, potential, and mass distribution (Binney & Merrifield 1998); therefore, stellar kinematics is a mass probe. The application of measuring rotation curves are multiple: they can be used to study kinematics, evolutionary histories of galaxies, and departures from Keplerian for the possible existence of the dark matter (Sofue & Rubin 2001). However, measuring the Milky Way rotation curve is challenging because of the observation constraints caused by our location in the Milky Way. Our line of sight is blocked by the dust in the disk, so we can not observe stars far from the Sun in the disk plane. The fact

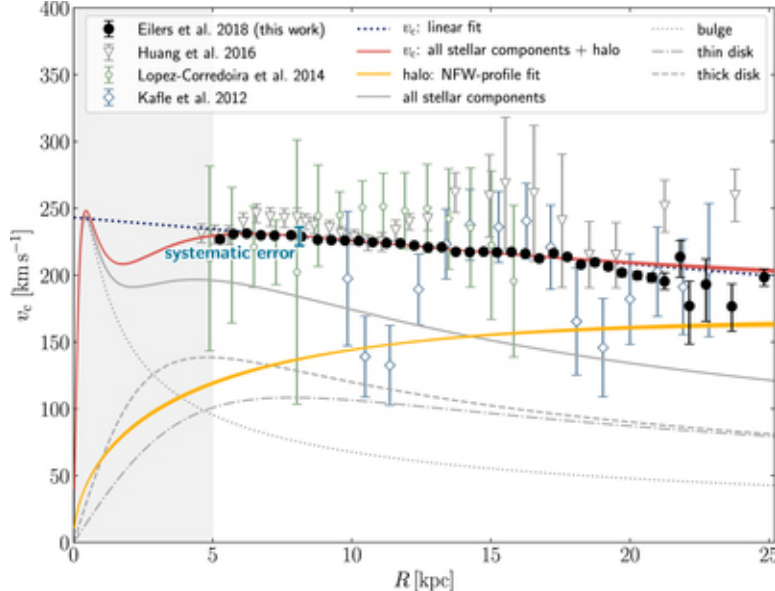


Figure 1: Recent measurements of the circular velocity curve of the Milky Way. The red curve is an approximated overall rotation curve (Eilers et al. 2019).

that we are co-moving with the Galaxy means rotation velocity can only be deduced from the relative motions of stars and gases.

Various tracers and methods have been used to track the rotation curve. Determining the distances of tracers are always difficult for astronomers due to the extinction from interstellar medium. For the inner region within the Sun, the MW rotation curve has been determined via the tangent-point method which uses the line of sight velocity of the gas clouds in CO, H I, and H II regions along certain observational directions measured from the shifts in the emission lines under Doppler's effect (Levine et al. 2008). Based on geometric and trigonometric derivations, this method is able to determine distances and rotation velocity just from the terminal radial velocities of gas clouds in a fixed direction with respect to the observer. The maximum line of sight velocity in a fixed observational direction corresponds to the circular velocity at the radius of the tangent point from the Galactic center. By sweeping through many different observational angles, we can map out the function of circular velocity against different radius. The rotation curve of the outer region beyond the Sun has been measured by other tracers, such as classical Cepheid (Joy 1939; Metzger et al. 1998; Mróz et al. 2019), RR Lyrae stars (Wegg et al. 2019), and luminous red giant stars (Eilers et al. 2019). Both classical Cepheids and RR lyrae stars are better for determining rotation curve because they are intrinsically bright and their distance-period relationship make distance measurement more reliable (Metzger et al. 1998).

1.2. Oort constants

While many methods to obtain constraint on the rotation curve require difficult observational measurements across a very large space, we can use the Oort constants

to measure local rotational properties. The Oort constants A and B (which are explained more in section 1.3 below) tell us the circular velocity around the Galactic Center and the slope of the rotational curve near the Sun's orbit (Binney & Merrifield 1998). Meanwhile, the sum of the other two Oort constants, K and C , gives the gradient of radial velocity about the GC at the Sun. The power of the Oort constants is that they are local parameters, but they enable us to test against different rotational models from their predicted values of circular velocity, slopes of circular and radial velocity. This work looks at the Oort constants in the vicinity of our Sun. An accurate measurement of the Oort constants in this region will potentially help us determine the local rotation curve, Galactic radius, and rotational velocity of the Sun (Olling & Merrifield 1998), as well as the eccentricity of the solar orbit (Kuijken & Tremaine 1994; Metzger et al. 1998).

To study the local rotation near the Sun and the Oort constants requires an understanding of Galactic coordinates. They are in a spherical coordinate system, with the Sun at its center and its plane parallel to the Milky Way midplane. Galactic longitude l is the counter-clockwise azimuthal angle measured from the Galactic center at $l = 0$, and the Galactic latitude, b , is the elevation angle from the MW plane (See Fig. 2). However, because the Sun actually moves in a non-circular orbit about the GC, it makes calculation unnecessarily complicated. We define a hypothetical reference point, Local Standard of Rest (LSR), as the reference frame in Galactic coordinates. The LSR is at the same instantaneous position of the Sun but moves on a circular orbit at 240 km s^{-1} . The relative motions of the Sun with respect to this LSR is described by peculiar motion, (u_0, v_0, w_0) , velocities in the radial, tangential and vertical directions, respectively (Binney & Merrifield 1998).

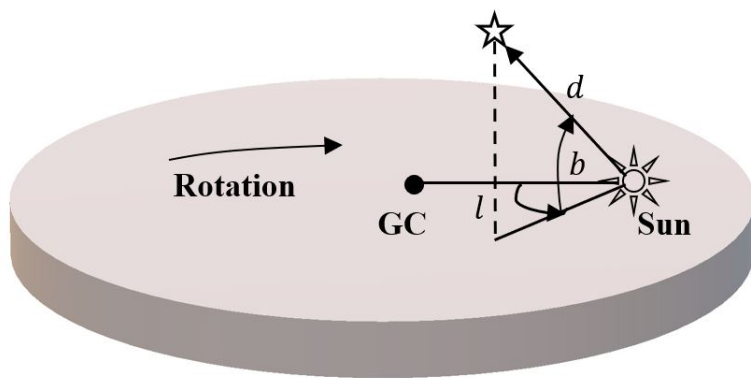


Figure 2: A sketch of the Galactic coordinate system.

Assuming the Milky Way has axisymmetric potential and stars are on circular orbits, Oort (1927) derived Oort constants A and B via radial velocities and tangential proper motions as a function of Galactic longitude l by Taylor-expanding the local

velocity field to the first order about the LSR. It is shown that the radial velocity, v_r , and tangential velocity, v_\perp , are proportional to $\cos 2l$, $\sin 2l$:

$$v_r = Ad \sin 2l \quad \text{and} \quad v_\perp = d(A \cos 2l + B), \quad (1)$$

$$\text{where } A = -\frac{1}{2}\left(\frac{dv_{circ}}{dR} - \frac{v_{circ}}{R}\right)\Big|_{R_\odot} \quad \text{and} \quad B = -\frac{1}{2}\left(\frac{dv_{circ}}{dR} + \frac{v_{circ}}{R}\right)\Big|_{R_\odot}.$$

In Oort's original measurement, he determined that near the Sun $A \approx 19$ (km/s/kpc) and $B \approx 24$ (km/s/kpc) (Oort 1927). The value, A describes the shearing, and B describes vorticity in the velocity field near the Sun. The result of a non-zero A suggests that stars near the Sun have varying rotation angular velocity, providing the first strong evidence that the Milky Way is rotating differentially.

The Oort constants are generalized to consider the Sun's peculiar motion with respect to nearby stars. It is derived analytically that the double sine (or cosine) trend is distinguishable from the pattern due to the Sun's peculiar motion about nearby stars. Two additional constants were introduced to the function of radial and tangential velocity against l , namely C , and K (Ogrodnikoff 1932). These four constants, A , B , C , and K describe the transverse shear, vorticity, radial shear, and divergence in the local velocity field accordingly. The line of sight velocity (v_{los}) is:

$$v_{los} = d(K + C \cos 2l + A \sin 2l) \quad (2)$$

The proper motion in longitude and latitude direction, μ_l and μ_b , have the following dependence on l (Olling & Dehnen 2003):

$$\mu_l = (A \cos 2l - C \sin 2l + B) \cos b \quad (3)$$

$$\mu_b = -(A \sin 2l + C \cos 2l + K) \sin b \cos b \quad (4)$$

if we assume the Sun only has circular motion.

From definition of A and B in Eq. 1, the local slope of the rotation frequency (Ω) at the solar radius, $\frac{d\Omega}{dr}|_{R_\odot}$ is $-(A + B)$. A and B are also related to the local rotation frequency by: $A - B = \Omega_\odot = \frac{v_{circ\odot}}{R_\odot}$ at the solar radius. The slope of radial velocity is given by the sum of K and C . If the Galaxy is not axisymmetric, C and K are nonzero (Ogrodnikoff 1932, Binney & Merrifield 1998). In the Method section below, I will present the full derivation of Oort constants. The Fourier series approximation approach has also been used to derive Oort constants. The Fourier coefficients of the $n = 0$ and $n = 2$ modes correspond to Oort Constants (Lin et al. 1978).

It must be emphasized that Oort constants can be extended to a set of functions depending on the distances from the Galactic center as we apply Taylor expansion to the velocity field about different locations in the MW. Typically, the Oort constants vary at a rate of a few km/s/kpc per kpc (Olling & Merrifield 1998). For distant stars in the disk, a higher order of the streaming velocity field equation must be taken into consideration (Siebert et al. 2011). The Oort constants in the first order of

the streaming velocity field equation are restrained to the rotation in the solar vicinity because the higher-order contributions will become significant at large distances (Bovy 2017). Due to the contribution from interstellar gas in the MW whose density varies non-monotonically with distance from the Galactic center between $0.9R_\odot$ and $1.2R_\odot$, the Oort constants $A(R)$ and $B(R)$ with varying R differ significantly from the general angular frequency dependence (Olling & Merrifield 1998). This suggests that when measuring the Oort constants, it is crucial to constrain the range of Galactic distance.

1.3. Measuring Oort constants

In order to measure the Oort constants based on Eqs. 2,3 and 4, we need to have locations and velocities of stars in Galactic coordinates. From our vantage point on Earth, we can get the stellar radial velocities from the Doppler shift, and proper motions are measured optically by tracing the stars moving across the plane in the sky. Positions, radial velocities, and proper motions are then converted to Galactic coordinates.

Many investigations have been conducted to attempt to use the proper motions in Galactic coordinates to determine the property of the non-uniformity in rotation and to measure the Oort constants. Fig.3 shows one example of the measurement of Oort constants with proper motions from (Bovy 2017). However, not all the results are in agreement, which is mainly due to the absence of a complete proper motions catalog. A complete measurement of proper motions can give us stars distant enough that their individual random motions do not dominate general trend of the proper motions. It will also ensure sufficient sky coverage to allow the separation between the double sine curve of Galactic proper motions from the single sine curve due to the solar peculiar motion in Eqs. 2, 3 and 4 (Kerr & Lynden-Bell 1986). Although the observational precisions have been continuously developed, the values of A and B are still consistent within uncertainties in different previous investigations. However, for the values of C and K , the measurement uncertainties are generally large (Li et al. 2019). Besides needing a complete proper motion catalog, three other factors further complicate an accurate determination of values for the Oort constants.

First, the effect of non-axisymmetric potential associated with the spiral arms or bar structure is not taken into account in Oort's model. Observation data suggest the necessity of looking at a non-axisymmetric mode (Metzger et al. 1998). From the radial velocity of Cepheids, a significant zero-point offset in Eq. 2 (the Oort constant, K) in the radial velocities suggests for a non-axisymmetric model. Metzger et al. (1998) also found a positive antisymmetric ellipticity component at R_\odot . The deviations from the general axisymmetric velocity field, or the deviation from the Oort constants model specified by Eqs. 2, 3 and 4, could be used to study the non-circular motions in great detail and infer the mass associated with the spiral arms (Olling & Merrifield 1998).

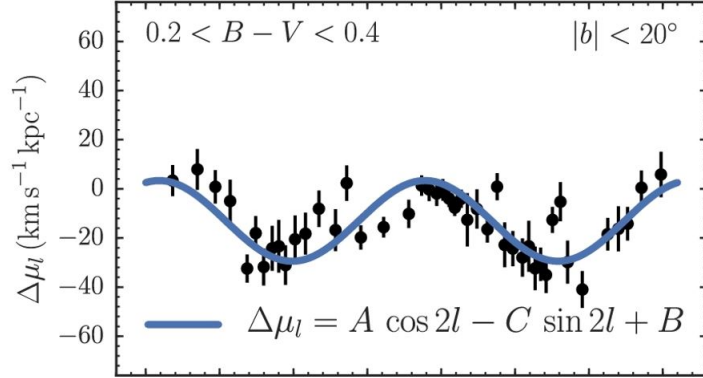


Figure 3: One example of the previous measurement of Oort constants from Bovy (2017) with observed proper motion in Galactic longitude: the value on y -axis is corrected for the solar peculiar motion based on Eq. 3. The averages $\mu_l(l)$ binned by l and their errors are plotted.

Second, it is found that moderate strength in the spiral structure causes errors of order 5 km/s/kpc in A and B (Minchev & Quillen 2007). The spiral structure can be understood as density waves where the spirals have concentrated stars. The streaming motion caused by density waves depending on the local spiral structure is difficult to determine (Lin et al. 1978). Further, the spiral structure raises the level of random motions in the Galactic disk (Sellwood & Carlberg 2014). Determination of other structural parameters to account for the effects from the Milky Way spirals must be made after a basic circular model in Section 1.2.

Third, the nonuniform distribution of stars with measured parallax over longitude in conjunction with the solar peculiar motion contributes to significant $n = 0$ and $n = 2$ modes deviated from the first order Oort analysis using Fourier series approximation (Olling & Dehnen 2003). The nonuniform distribution of stars across l may be due to intrinsic density nonuniformity or observational errors due to the interstellar extinction. This systematic error has a contribution to the longitudinal proper motion $\mu_l(l)$ indistinguishable from the effect of double \sin and \cos dependency. Olling & Dehnen (2003) suggested using the latitudinal proper motions $\mu_b(l)$ of stars at low latitudes could correct for the errors from mode mixing in Fourier approximation.

1.4. Recent progress based on *Gaia* data

In previous decades, the HIPPARCOS telescope had been used extensively in studying the MW kinematics, including deriving local Oort Constants and the rotation curve from classical cepheid (Feast & Whitelock 1997, Mignard 2000, Olling & Dehnen 2003). The *Gaia* (Global Astrometric Interferometer for Astrophysics) mission (Gaia Collaboration et al. 2016a) has collected astrometric parameters with unprecedented accuracy and multitude since the European Space Agency launched it in 2013. It aims to build a three-dimensional map of our Galaxy. By the second release of *Gaia* data, we have the parallax and proper motions measurements of over

1.6 billion stars (Gaia Collaboration et al. 2018). This also includes stars in higher latitude with significant latitudinal proper motion. Therefore, *Gaia*’s large set of astrometric measurements allows the first truly local precise measurement of the Oort constant and investigation of fine local kinematic features.

Two studies using *Gaia* DR1 and DR2 to calculate the Oort Constants in the solar vicinity yielded results in agreement (Bovy 2017; Li et al. 2019). The current values of the Oort constants based on DR2 are $A = 15.1 \pm 0.1$, $B = -13.4 \pm 0.1$, $C = -2.7 \pm 0.1$, $K = -1.7 \pm 0.2$, in the unit of km/s/kpc (Li et al. 2019). The slope of the rotation curve determined from $-(A + B)$ is negative, thus confirming a slightly declining rotational curve in the solar vicinity. And significant non-zero C and K further indicate non-axisymmetric potential (Bovy 2017; Li et al. 2019). This suggests that applying the axis-symmetric assumption of Oort’s analysis should be carefully examined. Both studies found the local Oort constants varied among different stellar populations based on their positions in the Hertzsprung-Russell Diagram (i.e. stellar age). The result in Li et al. (2019) shows that the red giants deviate from the main-sequence stars in all four constants because they show more elliptical orbits and larger velocity dispersions. However, this finding is inconsistent with the suggestion in Olling & Dehnen (2003) that red giants are the “true” tracer of the Oort constants because they are old enough to be in equilibrium and distant enough to be unaffected by possible local anomalies. This disagreement suggests establishing an appropriate set of stars is critical to determine Oort constants accurately.

Neither of the previous works using HIPPARCOS and *Gaia* data to derive Oort constants (Bovy 2017, Li et al. 2019) used radial velocities, because the radial velocity measurement are only available for a fraction of the stars in the *Gaia* data. However, we believe that a closer look at the available radial velocity data with comparison to the predicted theoretical model potentially entails significant information.

1.5. Motivation of the research

Our work focuses on the main sequence stars from *Gaia* DR2. We use their latitudinal and longitudinal proper motions, as well as their radial velocities to determine the local Oort constants in the solar vicinity.

In order to measure Oort constants to higher precision and to understand the influence of sample selection on the final results, this work examines the conventional constraints on data sampling by combining the observational data and numerical simulations. In previous measurements of the Oort constants (Olling & Dehnen 2003; Bovy 2017; Li et al. 2019), the sampling limit on parallax and latitude were explained qualitatively without justification. For example, Olling & Dehnen (2003) suggested to use the longitudinal profile μ_b of low latitudes stars to correct for the mode-mixing in deriving the Oort constants mentioned in Section 1.3, while both Bovy (2017) and Li et al. (2019) adopted the $40^\circ < |b| < 50^\circ$ filtering criteria. Therefore, it is not clear, especially in the case of analyzing μ_b , which subsets of stars in observation data

should be used to derive the Oort constants and how using different subsets affects the final results.

We use a simple 3D toy model of simulated test particle under the near circular orbital motion assumption to obtain a theoretical prediction of longitudinal and latitudinal proper motion, μ_l and μ_b , and radial velocity v_{los} as functions of Galactic longitude l . The goal of this model simulation and comparing it to observational data is twofold. First, it allows us to find the range of parallax and Galactic latitude that give the best stellar subset(s) for Oort constants measurement. Second, it helps us to characterize the deviations in *Gaia*'s observational result from the expected model. The larger significance of this work is to provide a sample selection guidance for future Oort constants analysis.

In addition, to derive the Oort constants and their uncertainties, this work applied the Monte Carlo Markov Chain (MCMC) method for both observational results from *Gaia* and the simulation results of the toy model to Eqs. 2, 3 and 4. Details of the sample selection, MCMC fitting, and simulation are included in the following sections. In the result section, we explore the connection between our simulation and DR2 observational data. We hope that the result of this work will give some guidance and insights into deriving the Oort constants from more complete catalogues in the near future, for example, the recent *Gaia* early third data release of *Gaia* in December 2020 (Gaia Collaboration et al. 2020).

2. METHODS

2.1. Derivation of The Oort constants

The Oort constants describe stellar streaming motions about the Sun in the Galactic coordinate, a left-handed coordinate where the direction from the Sun to the Milky Way (MW) galactic center is longitude $l = 0$ (Fig. 2). Considering a flat 2D Galactic disk under axisymmetric potential and all stars move on near circular orbits, e.g. as defined in Olling & Dehnen (2003). The position of a star on the disk is (x, y) , where $(0, 0)$ is at the Sun in the Galactic coordinate. The velocity field $\langle v \rangle$ gives the average velocity at each point on the disk. Assuming the Sun is on a pure circular orbit, in the solar vicinity, the velocity at (x, y) may be expanded in a Taylor series about the Sun:

$$\langle v \rangle|_{(x,y)} = \langle v \rangle|_{(0,0)} + \begin{pmatrix} v_{xx}, v_{xy} \\ v_{yx}, v_{yy} \end{pmatrix} \Bigg|_{(0,0)} \begin{pmatrix} x \\ y \end{pmatrix} \quad (5)$$

$$= \langle v \rangle|_{(0,0)} + \begin{pmatrix} K + C, A - B \\ A + B, K - C \end{pmatrix} \Bigg|_{(0,0)} \begin{pmatrix} x \\ y \end{pmatrix}, \quad (6)$$

where A, B, C and K are the Oort constants. The relative velocity of the star as observed from the Sun is given by

$$\delta\langle v \rangle|_{(x,y)} = \langle v \rangle|_{(x,y)} - \langle v \rangle|_{(0,0)}. \quad (7)$$

The line of sight velocity is the component of $\delta\langle v \rangle$ parallel to the distance vector d between the Sun and the star:

$$v_{los} = \hat{d} \cdot \delta\langle v \rangle = \frac{(x, y)}{d} \cdot \begin{pmatrix} K + C & A - B \\ A + B & K - C \end{pmatrix} \Big|_{(0,0)} \begin{pmatrix} x \\ y \end{pmatrix}. \quad (8)$$

After taking the dot product and applying trigonometric relations, we have

$$v_{los} = d[K + A \sin 2l + C \cos 2l] \quad (9)$$

Similarly, the longitudinal proper motion, perpendicular component of the relative velocity over d , is:

$$\mu_\perp = \frac{1}{d}(\hat{d} \times \delta\langle v \rangle) = B + A \cos 2l - C \sin 2l \quad (10)$$

Because the Sun has non circular velocity components, Eqs. 9 and 10 in fact describe the motions relative to the LSR. After correcting the solar peculiar motion, the two equations turn into:

$$v_{los} = d[K + A \sin 2l + C \cos 2l] - u_0 \cos l - v_0 \sin l \quad (11)$$

$$\mu_l = \cos b(B + A \cos 2l - C \sin 2l) + \frac{1}{d}[u_0 \sin l - v_0 \cos l], \quad (12)$$

where the $\cos b$ term in Eq. 12 accounts for the projection of distance onto the Galactic plane in a 3D MW disk. If the vertical velocity v_z of the star is non-zero, the latitudinal relative velocity at (l, b, d) is given by $v_z \cos b - v_{los} \sin b$ (Olling & Dehnen 2003), and the latitudinal proper motion is:

$$\mu_b = -(A \sin 2l + C \cos 2l + K) \sin b \cos b + \frac{1}{d}[(u_0 \cos l + v_0 \sin l) \sin b - w_0 \cos b], \quad (13)$$

where ϖ is parallax and its inverse gives the distance of the star from the Sun.

2.2. The Gaia Sample selection and stellar parameter estimation

The *Gaia* mission of the European Space Agency (ESA) surveys about one billion stars in the MW photometrically and spectroscopically to make the most accurate three-dimensional map of the Galaxy. In 2018, ESA released the second intermediate data DR2. This version of release catalogs the positions, proper motions, and other photometric data of 1.6 billion entries. *Gaia* samples kinematic tracers to a magnitude limit of at least $G = 20$ mag in the MW disk, bulge, and halo. The instrument package of *Gaia* spacecraft comprises two identical optical telescopes (or imaging systems), a radial velocity spectrometer, and blue and red photometers. The unfiltered, white-light photometric G band of the optical telescope covers 330–1050 nm (Gaia Collaboration et al. 2016). The parallax uncertainties are 0.5 mas at $G = 20$. The uncertainties in proper motion are 0.5 mas/yr at $G = 20$ (Gaia Collaboration et al. 2018).

The radial-velocity spectrometer obtains radial velocities by measuring the Doppler-shift in the lines of stellar spectra. DR2 has the radial velocity of more than 7.2 million stars with a mean $G = 4 - 13$ mag and an effective temperature in the range 3550 to 6900 K. The overall precision of the radial velocities range from 200-300 m/s to 1.2-3.5 km/s ([Gaia Collaboration et al. 2016](#)). Astrophysical parameters such as effective temperature, surface gravity, metallicity of the stars, and extinction are derived from the BP and RP data measured by the blue and red photometers over the wavelength ranges 330–680 nm and 630–1050 nm ([Gaia Collaboration et al. 2016](#)). In December 2020, ESA made the third early data release (EDR3) which added more than 100 million entries to the original DR2 catalogue. We used the TAP service from TOPCAT (Tool for Operations on Catalogues And Tables) to access, process, and select the DR2 data ([Taylor 2005](#)). (Appendix 6.1 includes preliminary results on EDR3.)

In Eq. 6, since the first-order Taylor approximation is only appropriate for the solar vicinity, the stellar samples are limited to the region within 500 pc (2mas) from the Sun. And restricting parallax/error ≥ 10 will avoid additional bias from inverting the parallax to estimate distances ([Luri et al. 2018](#)). The uncertainties in the BP and RP fluxes are constrained to less than 10% in making the Hertzsprung–Russell (H-R) diagram and selecting the main sequence samples which is shown in Figure 4. Potential duplicate sources are also removed. In sum, the query criteria in TOPCAT are the following:

```
parallax > 2,  parallax/parallax_error > 10,
phot_BP_mean_flux_over_error > 10,  phot_RP_mean_flux_over_error > 10,
duplicated_source = 0
```

The main sequence stars are selected by drawing on the H-R diagram in TOPCAT after parallax, color excess and extinction correction in Fig. 4. Because the local Oort constants varied among stellar populations of different colors and their collective kinematic properties, we group the main sequence stars into six color groups on the H-R diagram according to the criteria of [Li et al. \(2019\)](#). The rotational kinematics properties and the corresponding Oort constants for color group are analyzed individually. Table1 shows the number of stars in each stellar group in DR2.

Table 1: Number of main sequence stars that fall into each color group in DR2.

$BP - RP - E(BP - RP)$	< 0.8	$0.8 - < 1.2$	$1.2 - 1.6$	$1.6 - < 2.0$	$2.0 - 2.4$	≥ 2.4
DR2	978428	1591020	1284402	1086626	865742	351820

The proper motions and radial velocity entries in *Gaia* are measured in the equatorial coordinates system (ICRS), i.e. right ascension (α) and declination (δ) proper motions, μ_α and μ_δ . I used the SkyCoord class in *astropy* ([Astropy Collaboration](#)

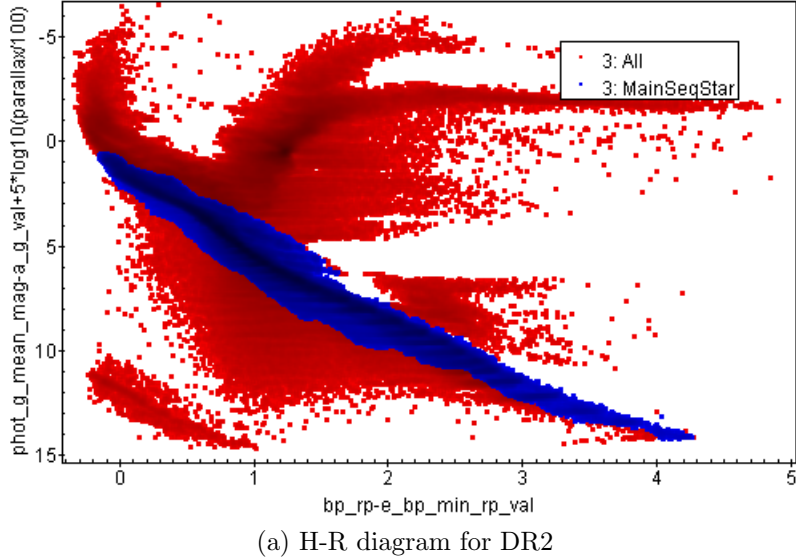


Figure 4: The Hertzsprung–Russell (H–R) diagram of stars within 500pc from the Sun in Gaia DR2 after parallax, extinction and color excess correction. Stars belong to the main sequence is highlighted in blue.

et al. 2018) to transform proper motions and available radial velocity from ICRS to the Galactic coordinate. The units of proper motion are also converted from mas/yr to km/s/ kpc by multiplying a factor of 4.74047.

2.3. Estimating the Oort constants from Gaia DR2 data

For each stellar group in Table1, we use the following process to derive the corresponding Oort constants from μ_l , μ_b and v_{los} .

We first convert the proper motions and radial velocities from ICRS to the Galactic coordinates. As we will see in the result section, μ_l is the more reliable tracer to derive the Oort constants, and only the first two bluest color groups have v_{los} measurement available for most of the entries. Rearranging Eq. 12, we define $\Delta\mu_l$ as :

$$\Delta\mu_l = \frac{1}{\cos b}(\mu_l - \varpi(u_0 \sin(l) - v_0 \cos l)) = A \cos 2l + B \sin 2l + C. \quad (14)$$

We use all the individual μ_l to find the solar peculiar motion (u_0, v_0, w_0) such that the binned medians of $\Delta\mu_l$ with bin width of $l = 5^\circ$ after removing any outlying values fit to $A \cos 2l + B \sin 2l + C$ by maximum-likelihood estimation method. Eq. 14 constrains the value of u_0 and v_0 in the solar peculiar motion, but not for w_0 . Therefore, we use $w_0 = 7.25$ km/s from Schönrich et al. (2010) together with the u_0 and v_0 estimated from $\Delta\mu_l$ above to find $\Delta\mu_b$ and Δv_{los} by rearranging Eqs. 13 and 11:

$$\Delta\mu_b = -\frac{1}{\sin b \cos b}(\mu_b - \varpi[(u_0 + v_0) \sin b - w_0 \cos b]) = A \sin 2l + C \cos sl + K, \quad (15)$$

$$\Delta v_{los} = \varpi(v_{los} + u_0 \cos l + v_0 \sin l) = A \sin 2l + C \cos sl + K. \quad (16)$$

Then we estimate the Oort constants from $\Delta\mu_l$, Δv_{los} and $\Delta\mu_b$ respectively.

2.4. Estimating the parameters and their corresponding uncertainties: Monte-Carlo-Markov-Chain

In Eqs. 14, 15 and 16, each model is parameterized by three of the four Oort constants. When we consider $\Delta\mu_l$ and $\Delta\mu_b$ together in estimating the Oort constants, the model parameters are the four Oort constants. For such a high-dimensional parameter space, we use the Monte Carlo Markov Chain (MCMC) method to determine the value and uncertainty of each parameter. The MCMC method combines our prior knowledge about the model and evidence from the data to obtain a posterior distribution of the model parameter θ , in this case, $\theta(A, B, C)$, (A, C, K) or (A, B, C, K) .

MCMC method randomly samples a parameter model from the parameter distribution based on our prior knowledge, and evaluate how our data is likely based on this particular model. This likelihood is called the posterior likelihood function. MCMC then uses the process of Markov chain to “walk” around the high-dimension parameter space until it finds the set of parameter values that maximizes the posterior likelihood function. The posterior combines a prior distribution on the model parameter θ and a logarithmic likelihood function that quantifies how well our data support the parameter model. For example, if we derive the Oort constants by considering $\Delta\mu_l$ and Δv_{los} together, the corresponding logarithmic likelihood function weighted by errors is defined as:

$$\ln \mathcal{L} = - \sum_i \left(\frac{(\langle \Delta\mu_l \rangle_i - y_{1i})^2}{\sigma_{\langle \Delta\mu_l \rangle}^2 + error_{\langle \Delta\mu_l \rangle i}^2} + \ln \frac{2\pi}{\sigma_{\langle \Delta\mu_l \rangle}^2 + error_{\langle \Delta\mu_l \rangle i}^2} \right. \\ \left. - \frac{\langle \Delta v_{los} \rangle_i - y_{2i}^2}{\sigma_{\langle \Delta v_{los} \rangle}^2 + error_{\langle \Delta v_{los} \rangle i}^2} + \ln \frac{2\pi}{\sigma_{\langle \Delta v_{los} \rangle}^2 + error_{\langle \Delta v_{los} \rangle i}^2} \right) \quad (17)$$

where $\sigma_{\langle \Delta\mu_l \rangle}$ and $\sigma_{\langle \Delta v_{los} \rangle}$ are the Gaussian scatter for the distribution of binned medians, $error_{\langle \Delta\mu_l \rangle i}$ and $error_{\langle \Delta v_{los} \rangle i}$ are the standard deviations within each bin, and y_1 and y_2 are given by Eqs. 14 and 16 (Li et al. 2019).

Based on the results of previous literature (Bovy 2017, Li et al. 2019), we use a step function for the prior distribution of θ :

$$P(\theta) = \begin{cases} 0 & \text{if } 10 < A < 20, -15 < B < -5, -5 < C < 5, \text{ and } -5 < K < 5 \\ -\infty & \text{if } A, B, C \text{ and } K \text{ are not within the range above} \end{cases} \quad (18)$$

And the overall logarithmic posterior probability is:

$$LnP(\theta|y) = \begin{cases} lnL & \text{if } P(\theta) = 0 \\ 0 & \text{if } P(\theta) = -\infty \end{cases} \quad (19)$$

MCMC uses multiple Markov chains that start at slightly different initial parameter values. All Markov chains eventually converge in the high probability region of the parameter space. We use the standard deviation of the final value of each parameter in θ after all Markov chains converge as the uncertainties of the derived Oort

constants. We employ the *emcee* (Foreman-Mackey et al. 2013) python package to sample and update the Markov chains in MCMC.

2.5. Test particle simulation

To know what behaviors are expected from the theoretical Oort constants model, and thus understand how the actual MW deviates from the theoretical model, we construct a toy model simulation, treating stars as test particles in a fixed MW potential. The simulation assumes all the model constraints of the Oort constants and the Sun stays on a circular orbit. We sample 500,000 of test particles from *AGAMA*'s quasi-isothermal distribution function to represent a thin 3D Milky Way galactic disk (Vasiliev 2019). The distance from the Sun to the Galactic center and the circular velocity at the solar radius are set to $R_0 = 8.34$ kpc and $v_0 = 240$ km/s respectively. The scale height of the disc is 0.4 kpc, and the radial velocity dispersion is chosen as 10km/s. These values give us an approximation for a thin MW disk under the cold limit. This distribution function provides planar and vertical profiles of the thin disc with analytic function dependent on the action integrals in an integrable, axisymmetric Hamiltonian (Binney 2010). The Galactic potential in the Hamiltonian is specified by MWPotential2014 (Bovy 2015).

MWPotential2014 serves as a simple and accurate model for the MW potential from fitting a large variety of dynamical data. This potential model consists of a bulge potential with a power law exponent of 1.8 and a cut-off radius of 1.9kpc (PowerSphericalPotentialwCutoff), a disk potential specified by MiyamotoNagaiPotential, and a dark-matter halo described by an NFWPotential (Bovy 2015). Fig. 5 shows the spatial distribution of test particles sampled from the quasi-isothermal distribution function.

Besides, because we set the peculiar motion of the Sun to zero, the coordinate and velocity of LSR and the Sun are equivalent. All particles undergo 10Gyr of orbit integration under the potential specified by MWPotential2014 to reach equilibrium. The positions and velocities after 10Gyr are then used to calculate μ_l and μ_b , as well as v_{los} . Similar to the procedure of analyzing *Gaia* data, the simulation data are binned by $l = 5^\circ$, and the binned medians are used to estimate the three equations in Eq 11, 12 and 13 by MCMC, except u_0 , v_0 , and w_0 are set to 0.

3. RESULTS

3.1. Simulation: The effect of sampling criteria on μ_l , v_{los} , μ_b

From the simulation with 500,000 stars (test particles) described above (Section 2.5), we examine the effect of different sampling criteria on the resulting proper motions (μ_l and μ_b) and the line-of-sight velocity (v_{los}) dependency on l . Fig 5a displays the distribution of all the particles in 16 kpc from the GC and ± 4 kpc in the vertical direction. In Fig 5b, we show those stars within $d = 3$ kpc from the Sun. We replicate the Sun's position at four symmetric positions (8.34kpc, 0, 0), (0, 8.34kpc, 0), (-8.34kpc, 0, 0) and (0, -8.34kpc, 0) in the Cartesian form of the Galactocentric

coordinate. This strategy increases the number of stars nearby the Sun(s) to give us robust results in deriving the Oort constants.

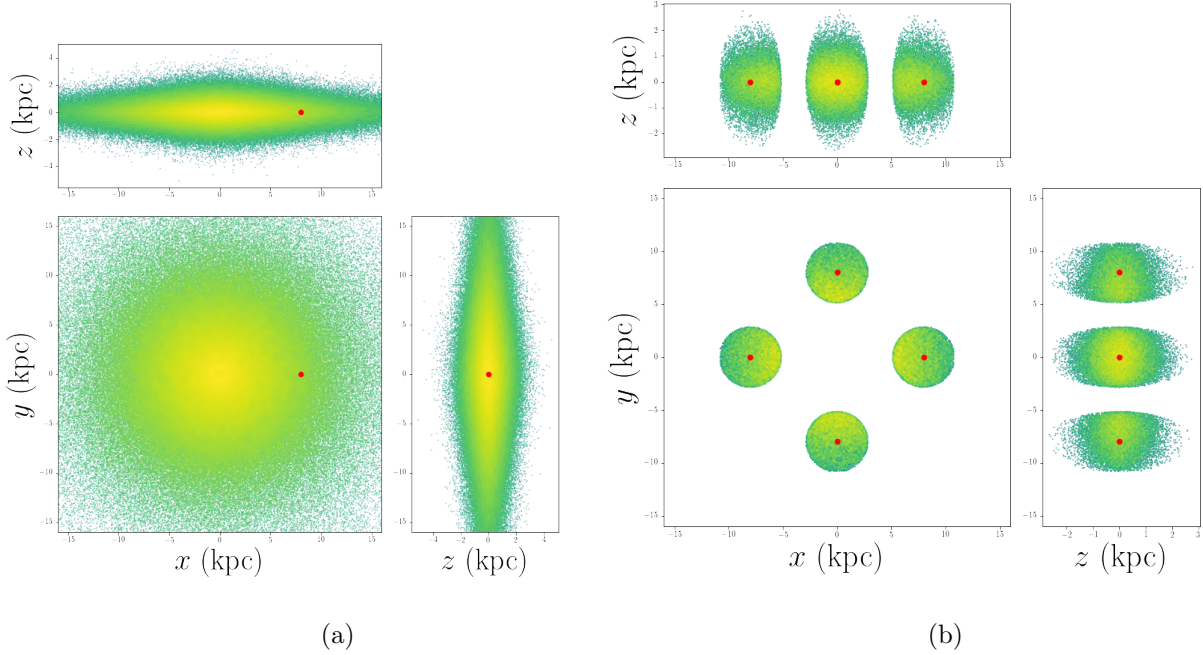


Figure 5: (a) The distribution of the 500,000 test particles (stars) sampled from quasi-isothermal distribution function for the Milky Way. (b) The distribution of simulated stars within $d = 3\text{kpc}$ from the Sun, where we replicate the Sun at four different symmetric positions to increase the sizes of effective samples near the Sun. Brighter color corresponds to a higher density.

3.1.1. Longitudinal profiles of μ_l and v_{los}

In Fig. 6, we present the result of μ_l vs l under three sample filtering criteria on the galactic distance d for stars that approximately lie on the mid-plane ($|b| < 20^\circ$). Proper motions after correcting the contribution in latitudinal direction ($\cos b$) are mostly negative across $l = 0^\circ$ to 360° , indicating that stars move in the decreasing l direction. Fig. 6 also shows that μ_l has slightly positive value at $l = 0^\circ, 180^\circ$, and 360° . μ_l is most negative and has relatively larger variation among the stars at $l = 90^\circ$ and 270° compared to the stars at $l = 0^\circ, 180^\circ$, or 360° . In Fig. 6a, the standard deviation of $\mu_l / \cos b$ at $l = 0^\circ$ is 0.54 km/s/kpc, and increases to 4.00 km/s/kpc at $l = 90^\circ$.

In Fig 7, we see for stars with $d < 2\text{kpc}$ and $|b| < 20^\circ$, v_{los} after divided by d traces a double sinusoidal function as expected from Eq. 11. v_{los} is 0 at $l = 0^\circ, 90^\circ, 180^\circ, 270^\circ$. Positive v_{los} between $l = 0^\circ$ to 90° and $l = 180^\circ$ and 270° suggests that stars move away from the Sun in the line of sight direction in these two l intervals. And stars

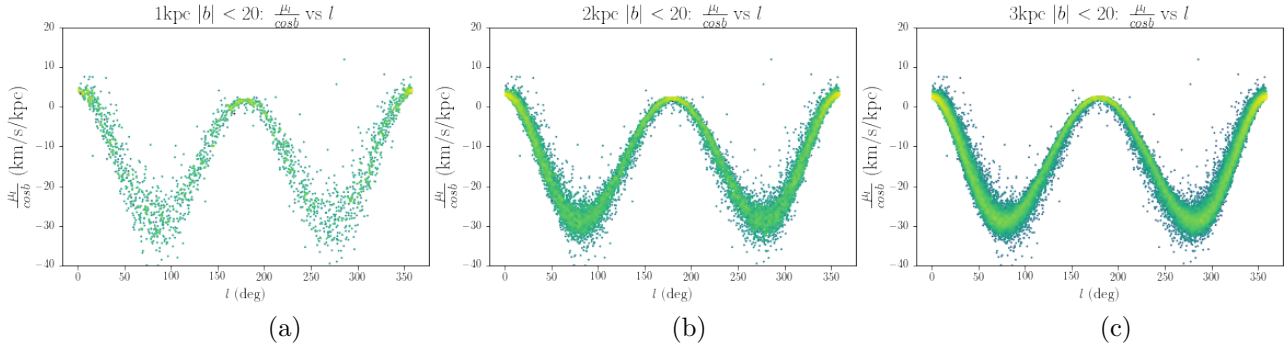


Figure 6: The distribution of $\mu_l/\cos b$ over l for stars with $|b| \leq 20$ and ,(a) $d \leq 1$ kpc,(b) $d \leq 2$ kpc, and (c) $d \leq 4$ kpc

approach the Sun in the line of sight direction between $l = 90^\circ$ and 180° , 270° and 360° . We show the comparison of v_{los}/d vs l if we keep $|b| < 20^\circ$ but constrain the stars within 1kpc in Fig. 7a and within 3kpc in Fig. 7c.

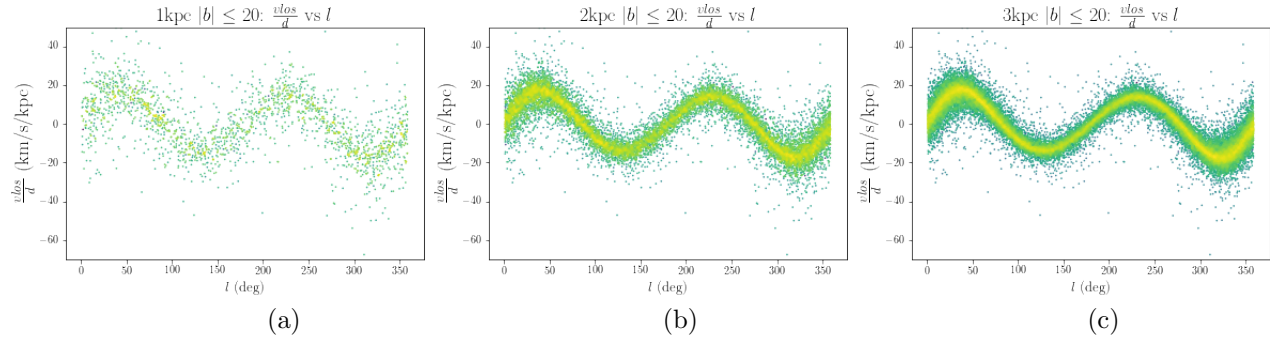


Figure 7: The distribution of v_{los}/d over l for stars with $|b| \leq 20$ and (a) $d \leq 1$ kpc,(a) $d \leq 2$ kpc, and (c) $d \leq 4$ kpc

In Fig. 8 , we use two simple schematic diagrams of stars in the solar vicinity to illustrate the expected variation of μ_l and v_{los} as a function of the Galactic longitude. We assume these stars are all in circular orbit around the GC. At $l = 0^\circ$ and 180° , v_ϕ is perpendicular to the line of sight. As a result, $v_{los} = 0$ and $v_l = v_\phi - v_{\phi\odot}$. According to the rotation velocity curve in (Fig. 1), the radial profile of v_ϕ is flat while slightly declining at $R = R_\odot$. As a result, the star moves in the direction of increasing l , giving μ_l a small positive value at $l = 0^\circ$ in the inner side of the MW disk. At $l=180$, because v_ϕ is smaller than $v_{\phi\odot}$, the star lags behind the Sun, moving in the direction of increasing l , thus μ_l is expected to be positive (Fig. 8b).

At $l = 90^\circ$ and 270° , stars are approximately in the same circular orbits as the Sun. They are essentially moving at the same speed as the Sun along the line of sight, thus $v_{los} = 0^\circ$. However, to examine their proper motion, we need to zoom in closer

to show that v_ϕ varies slightly in their direction. Fig. 8b shows the perpendicular component v_l points in the decreasing l direction at both $l = 90^\circ$ and 270° .

At $l = 45^\circ, 225^\circ, l = 135^\circ$ and 315° , the orange vectors in Fig. 8a and 8b indicate the relative velocity in the line-of-sight and tangential l direction after subtracting the velocity of the Sun in each direction respectively. We show that at $l = 45^\circ$, $v_{los} > 0$ and $v_l < 0$; $l = 45^\circ$, $v_{los} < 0$ and $v_l < 0$; $l = 135^\circ$, $v_{los} > 0$ and $v_l < 0$; $l = 225^\circ$, $v_{los} > 0$ and $v_l < 0$; $l = 315^\circ$, $v_{los} > 0$ and $v_l < 0$.

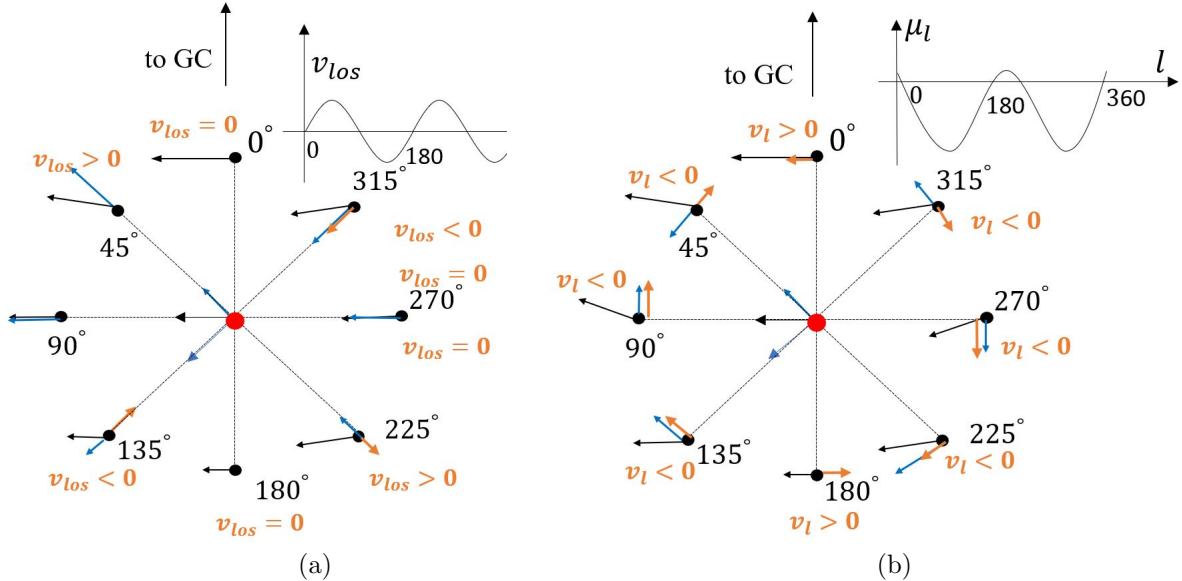


Figure 8: The variation in the radial velocity and transverse velocity among different Galactic longitude due to differential rotation of the Milky Way. The black arrows represent the velocity vector of v_ϕ . The blue vectors represent the components in the line-of-sight direction (Fig. 8a) and the longitudinal direction (Fig. 8b). The orange arrows are the relative velocity vectors in the two directions after taking the circular motion of the Sun into account.

3.1.2. The effect of the distance selection on the longitudinal profiles of μ_l and v_{los}

In Figs. 6 and 7, the number of samples selected drops from 51196 to 16741 and to 2310 as the galactic distance cut-off decreases from 3kpc, to 2kpc, and to 1kpc. While the dispersion of $\mu_l / \cos b$ and v_{los} / d are unaffected by the distance cut-off chosen in Fig. 6, the binned median values reveal some differences. In Fig. 9, all the scatter data of Fig. 6 are grouped into bins with a width of $l = 5^\circ$, and the median of μ_l in each bin is plotted against l . The error bars are the standard deviations in the corresponding bins. For simulated stars within 3kpc, although the general trend is similar to the $\cos 2l$ curves, there are non-negligible deviations from the double cosine function (Fig. 9c). This result suggests that 3kpc is too large for the first-order Taylor expansion around the Sun in Eq. 6. The stars within 2kpc yield a reduced

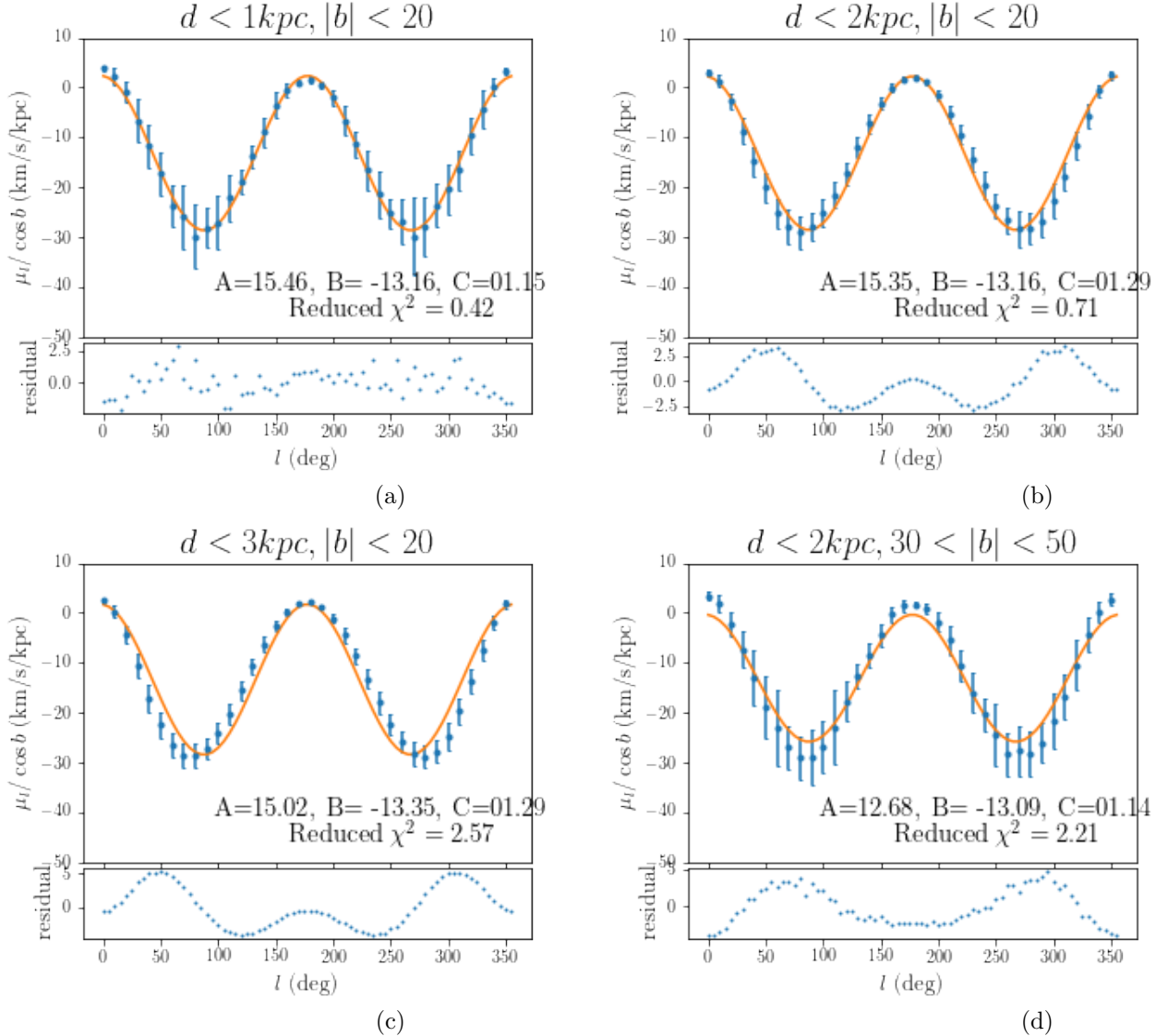


Figure 9: The function of binned median $\mu_l / \cos b$ over l for stars with $|b| \leq 20^\circ$ and (a) $d \leq 1\text{kpc}$, (b) $d \leq 2\text{kpc}$, and (c) $d \leq 4\text{kpc}$. The orange continuous curves come from fitting the binned median data to Eq. 12 with maximum likelihood approximation. Only 36 out of 72 binned medians are plotted. The bottom panel for each subplot includes the residual profile.

χ^2 closest to 1. The proper motions of stars within 1kpc from the sun trace the double sinusoidal function best compared to 2kpc and 3kpc, and the residuals are also smallest for this group. However, this galactic distance cut-off only yielded 2310 out of 500,000 that meet this filtering criteria. The standard deviation within each bin is larger possibly because a smaller sample size is more subjective to the larger difference between outlying values and the medians.

Similarly, the binned v_{los} median of stars within $d < 1\text{kpc}$ and $|b| < 20^\circ$ give v_{los}/d vs l closest to the function in Eq. 11 compared to the stars within 3kpc and 2kpc . The reduced χ^2 values calculated for all the fittings in Figs. 9 and 10 do not give informative measurements on the goodness of the fit. Reduced χ^2 being much larger than 1 suggests errors are underestimated, and overestimated for Reduced χ^2 being much smaller than 1. However for our simulated data, the errors come from standard deviation within each bin. Instead, we look at the range and distribution in the residual vs l profile to decide if the fit is satisfactory. For both $\mu_l/\cos b$ and v_{los}/d , the residual profiles for $d < 1\text{kpc}$ have the smallest ranges. Moreover, for the fittings of $d < 2\text{kpc}$ or $d < 3\text{kpc}$ samples, the residual distributions are not uniform above or below 0 but exhibit a clear dependency on l . While when $d < 1\text{kpc}$, residuals are distributed randomly above and below 0. The dependency of residuals on l seems worthy of further investigation in future work, as it may hint to additional velocity structures.

3.1.3. The effect of Galactic latitude range on the longitudinal profiles of μ_l and v_{los}

In the second column of Fig. 9, we compare the binned μ_l median vs l of stars at $d < 2\text{kpc}$ from the Sun but at different latitude ranges, $|b| < 20^\circ$ and $30^\circ < |b| < 50^\circ$. We constrain the samples to 2kpc because although stars within 1kpc give the best subset to estimate the Oort constants, there are not enough data with higher latitudes to compare the effect of different latitude cut-off. The scatter in the μ_l around the central double sinusoidal line increases for higher latitude regions as suggested by the error bars on the binned median data. When $|b| \leq 20^\circ$, stars are considered close to the MW mid-plane, thus are most suitable to fit the model in Eq. 12. For $30^\circ \leq |b| \leq 50^\circ$, not only the spread in the scattered data is larger, the binned medians deviate from the fitted double cosine function more significantly according to the residual vs l panel in Fig. 9.

Likewise, in Fig. 10, the spread in the v_{los}/d of the stars within 2kpc from the Sun but at a higher latitude b is larger. Comparing the residual profiles in the lower panels, we see the range of residuals is the smallest for the group closest to the MW mid-plane. This suggests that the deviation of binned v_{los}/d median from the predicted double sine function is smallest for stars at $|b| < 20^\circ$ and larger at $30^\circ < |b| < 50^\circ$. The result for stars with $60^\circ < |b| < 80^\circ$ is not shown in Fig. 9, we find their error bars and residuals are larger than the samples with $30^\circ < |b| < 50^\circ$. With a higher latitude constraint, we move away from the Milky Way disk, and the orbits get less circular. MW potential gradient in the z-direction is large enough to add significant vertical perturbations at high latitude region, tilting the circular orbits. Therefore, we expect that the deviation is significant for stars in high latitude regions in the solar vicinity.

3.1.4. Longitudinal profiles of μ_b

For proper motion in the latitude direction, μ_b , we expect to see more nonzero value at the region away from the Galactic plane with relatively larger latitude because of

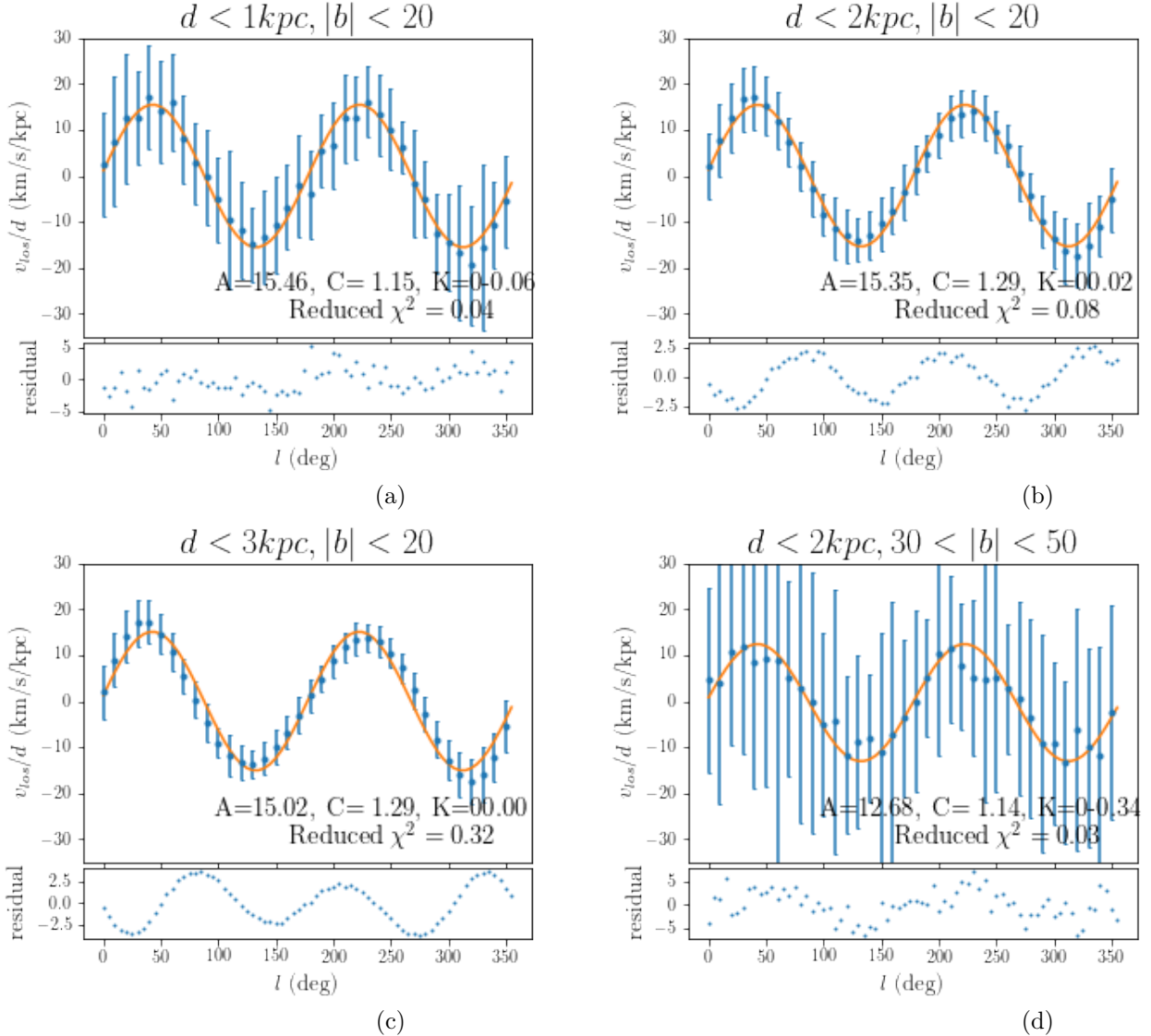


Figure 10: The longitudinal profiles of the binned median v_{los}/d over l for stars with $|b| \leq 20^\circ$ and (a) $d \leq 1\text{kpc}$, (b) $d \leq 2\text{kpc}$, and (c) $d \leq 4\text{kpc}$. The orange continuous curves come from fitting the binned median data to Eq. 11 with maximum likelihood approximation. Only 36 out of 72 binned medians are plotted.

the product $\sin b \cos b$ in Eq. 13. In Fig. 11, contrast to μ_l and v_{los} discussed above, the value of $\mu_b/\cos b \sin b$ of stars with $d < 2\text{kpc}$ and $30^\circ < |b| < 50^\circ$ are much more dispersed. Taking binned medians in Fig. 11 gives the double sinusoidal curve expected from Eq. 13. The binned standard deviations for these binned μ_b medians range from 50-100 km/s/kpc, much larger than the variation of the binned medians across l , ($\pm 25\text{km/s/kpc}$). At $l = 0^\circ, 90^\circ, 180^\circ, 270^\circ$, $\mu_b \approx 0$. Stars are descending from the perspective of LSR from $l = 0$ to 90° and from 180 to 270° while ascending from $l = 90^\circ$ to 180° and from 270° to 360° .

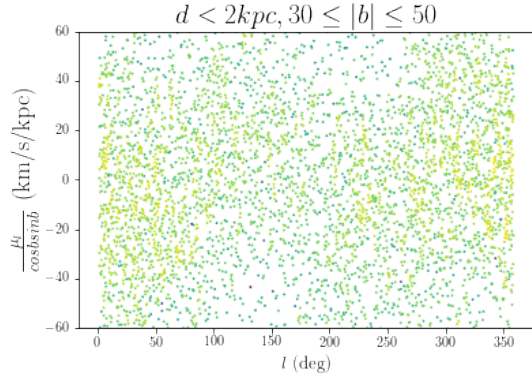


Figure 11: Longitudinal profiles of $\mu_b / \cos b \sin b$ for stars with $d < 2\text{kpc}$, $30^\circ < |b| < 50^\circ$ from simulation. All the individual data points are shown in this plot. There is no predicted double sinusoidal dependency on l until we use binned medians.

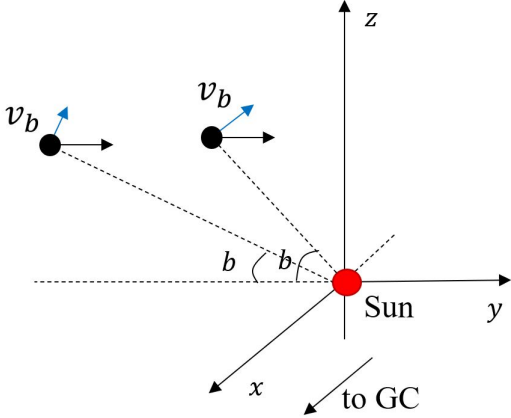


Figure 12: The change in latitude b and v_b with respect to the Sun for a star in a circular orbit at some vertical height over the MW mid-plane. In this hypothetical picture, the absolute height of the star does not change because v_z is set to 0, but its Galactic latitude changes as it approaches or moves away from the Sun.

Because the derivation of Oort constants assumes that stars are close to the MW mid-plane, the discussions on μ_l and v_{los} are more prevalent than the motion approaching or leaving the MW mid-plane. In fact, μ_b , the proper motion in the latitudinal direction is also a kinematic tracer of the MW differential rotation. In Fig. 12, we look at a star at some vertical distance from the MW mid-plane and on a hypothetical circular orbit with a constant v_ϕ and $v_z = 0$.¹ As this star rotates around the GC at a different v_ϕ than the Sun, its relative position with respect to the Sun changes, so it appears to approach or move away from the Sun while maintaining its height relative to the MW plane. The angle between the line-of-sight and the horizontal plane parallel to the Milky Way mid plane, which is just the Galactic latitude b , results in a $\sin b$ velocity component in the Galactic latitude b direction which is perpendicular to the line-of-sight, v_b . As illustrated in Fig. 12, this b angle varies when the star moves closer or away from the sun, so does v_b . Therefore, $\mu_b = \frac{v_b}{d}$ is also a tracer for the stellar in-plane motion. Its dependency on l can be used to derive Oort constants and study the differential rotation of the Milky Way. This component, v_b , is larger for stars with higher b because of the $\sin b$ component. Thus, in our simulation, we look at μ_b of stars with mid range b values. However, for stars with very high $|b|$, that is away from the disc in the vertical direction, their orbits are rather non-circular due to the potential perturbation in the vertical direction. These stars tend to have larger

¹ Such an orbital configuration is not physical. We only use it for the purpose of demonstrating the connection between μ_b and differential v_ϕ around the Milky Way center.

vertical velocities, which can give a more dominant contribution to μ_b than the effect coming from differential rotation discussed above.

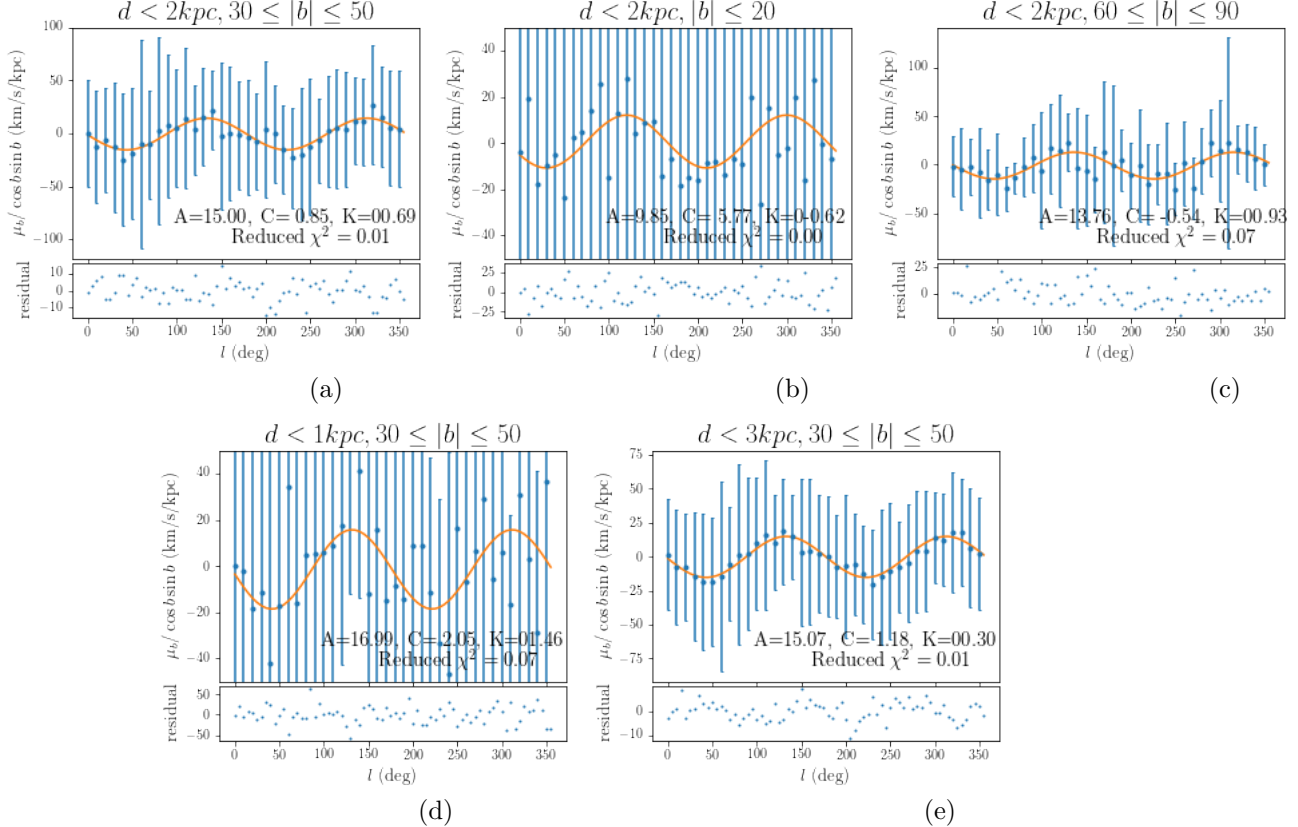


Figure 13: The function of binned median $\mu_b / \cos b \sin b$ over l for stars with different latitude and distance cut-off. On the first row $d < 2\text{kpc}$ and (b) $|b| \leq 20^\circ$, (a) $30^\circ |b| \leq 50^\circ$, and (c) $60^\circ |b| \leq 90^\circ$. The second row keeps $30^\circ |b| \leq 50^\circ$, while in (d) $d \leq 1\text{kpc}$, (e) $d \leq 4\text{kpc}$.

In Fig. 13, compared to the stars closer to the MW disk ($|b| < 20^\circ$) or those that are much farther away from the MW disk ($|b| > 60^\circ$), stars with $|b|$ between 30° and 50° yield the most noticeable double sinusoidal variation with l . In the residual profiles, the residuals for the group with $30^\circ < |b| < 50^\circ$ distribute randomly over the smallest range compared to the other two groups. This suggests that the group with $30^\circ < |b| < 50^\circ$ gives the most satisfactory fit to the model predicted by Eq. 13.

On the other hand, in the second row of Fig. 13, for larger spatial coverage, $d < 3\text{kpc}$, binned median of $\mu_b / \cos b \sin b$ shows a more evident double sinusoidal function than stars within 2kpc and 1kpc. The residual profile (bottom panels) suggests that the dispersion about the medians is the smallest when all the samples in a larger region around the Sun are included. This is likely due to the fact that for a larger sample size, the binned medians are less subjective to any extreme individual values. However, the trade-off for including more samples is applying the first-order

Taylor expansion in a much larger region than Sun vicinity, that becomes less accurate to describe the local kinematics.

3.2. The effect of radial and vertical velocity values on μ_l , v_{los} , μ_b

In Fig. 14, we include the longitudinal profiles of $\mu_l/\cos b$, v_{los}/d and binned median of $\mu_b/\cos b \sin b$ under different constraints on radial velocity v_r and vertical velocity v_z . On the top row, we artificially set $v_r = 0$, while $v_z = 0$ for the bottom row. The result shows the spread in μ_l is due to the variation of v_r . Both v_r and v_z make contributions to the scattering in v_{los}/d . When v_r is set to 0, the scattering around the central double sine curve is smaller as the brighter color indicates a higher density. However, comparing between Fig. 14b and 14d indicates the contribution to the scatter in v_{los}/d by v_z is more significant. The difference of the binned median of μ_b under three velocity profiles shows the deviation from the double sine function described by the Oort constants is attributed to the non-zero vertical velocity of stars, consistent with the discussion in section 3.1.4.

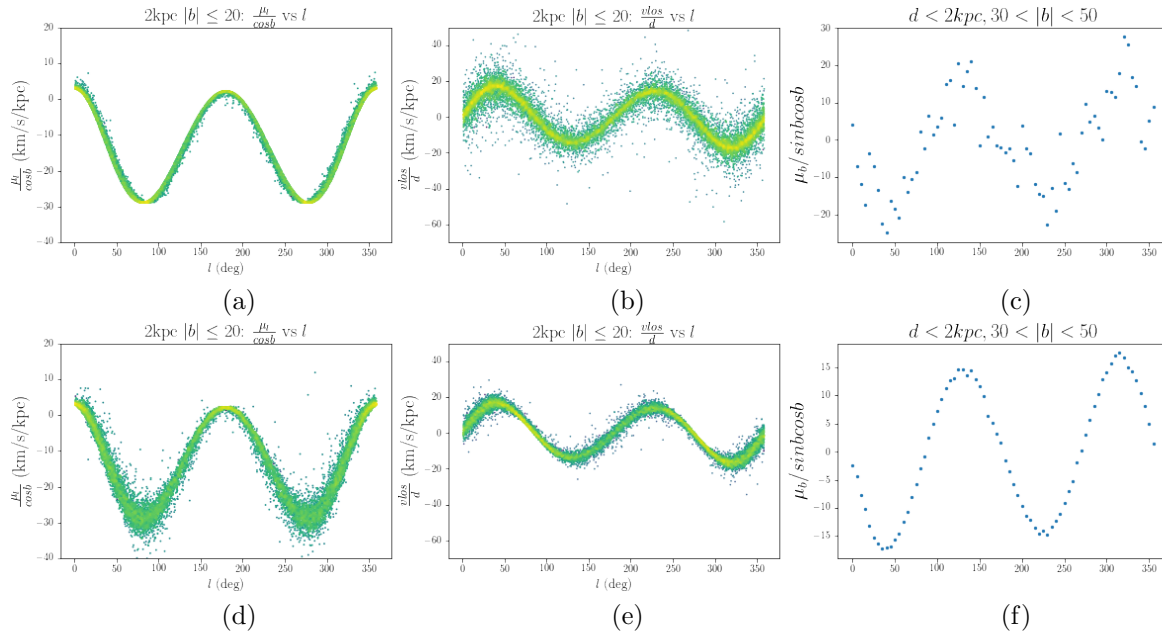


Figure 14: The longitudinal profiles of $\mu_l/\cos b$, v_{los}/d and binned median of $\frac{\mu_b}{\cos b}$ as a function of l and under two different velocity profiles. On the top row, $v_r = 0$, while on the bottom row, $v_z = 0$.

3.3. Gaia DR2 observational data

3.3.1. Gaia DR2: using the filtering criteria from literature

We now present the results using *Gaia* DR2 data described in Section 2. In Fig. 15, we show $\Delta\mu_l$ as a function of l in the region within $d < 500\text{pc}$ and $|b| < 20^\circ$ for stellar populations with $G_{BP} - G_{RP} - E(BP_RP) < 0.8$, $0.8 \sim 1, 2$, $1.2 \sim 1.6$,

$1.6 \sim 2.0$, $2.0 \sim 2.4$ and ≥ 2.4 . At least for the first three color populations, the binned medians of $\Delta\mu_l$ vs l fits Eq. 12. The deviations from the double cosine function are larger for redder stellar populations as we move across the panels from (a) to (d) in Fig. 15. This is consistent with the fact that redder stars are relatively older and under the subjection of potential perturbation for a longer time. This means their orbits are kinematically hotter with larger velocity dispersion. Thus, their motions are more deviated from circular. We also notice that there is a population of stars concentrated at $l = 290^\circ$ and μ_l around -20 km/s/kpc on the fitted function. We find the stars in this over dense region have smaller radial velocities values (Appendix Fig. 23a). This means the stars belong to this over dense region are the near circular and close to the Sun subset constrained by the Oort constant assumptions. Thus, their values of $\Delta\mu_l$ are around the line of the predicted function.

Similar to μ_l , v_{los} for the two bluest stellar population calculated from the radial velocity data in DR2 are also well described by the double sine function predicted by the Oort constants (Fig. 16). Despite that the radial velocity data not being available for all the stars in DR2, the two bluest stellar populations in Fig. 16 show that v_{los} can be used to derive the Oort constants. Table 2 shows the estimated peculiar motion (u_0, v_0) from fitting μ_l in Fig. 15 by maximum likelihood estimation.

Table 2: The value of the solar peculiar motion (u_0, v_0, w_0) such that the binned medians of $\Delta\mu_l$ in Fig. 15 fit to $A \cos 2l + C \sin 2l + B$. For w_0 , we adopt the value from Schönrich et al. (2010), $w_0 = 7.25 \text{ km/s}$ for all six groups.

$BP - RP - E(BP - RP)$	$u_0(\text{km s}^{-1})$	$v_0(\text{km s}^{-1})$
< 0.8	11.65	16.25
≥ 0.8 and < 1.2	11.10	18.61
≥ 1.2 and < 1.6	10.88	19.24
≥ 1.6 and < 2.0	10.46	18.70
≥ 2.0 and < 2.4	10.50	18.56
≥ 2.4	10.69	19.31

While the l dependencies of μ_l and v_{los} for the stars in DR2 are consistent with the equations of the Oort constants, μ_b for stars in the solar vicinity and intermediate $|b|$ range is a less accurate tracer to derive the Oort constants. Despite the binned medians of $\Delta\mu_b$ generally follow predicted the double sinusoidal curve except in the reddest population in Fig. 17f, the dispersion in $\Delta\mu_b$ is much larger than those in $\Delta\mu_b$ and Δv_{los} as evidenced by the error bars. This larger scatter in $\Delta\mu_b$ is not due to a smaller sample size like in our simulation, but the significant intrinsic vertical motions of the stars. This suggests that μ_b is a less reliable tracer for deriving the Oort constants.

Table 3 lists the values of the Oort Constants and their uncertainties estimated from the results in Fig. 15, 16 and 17 using MCMC. Δv_{los} is included in the two bluest group, while $\Delta\mu_b$ is included in the likelihood function for all but the reddest

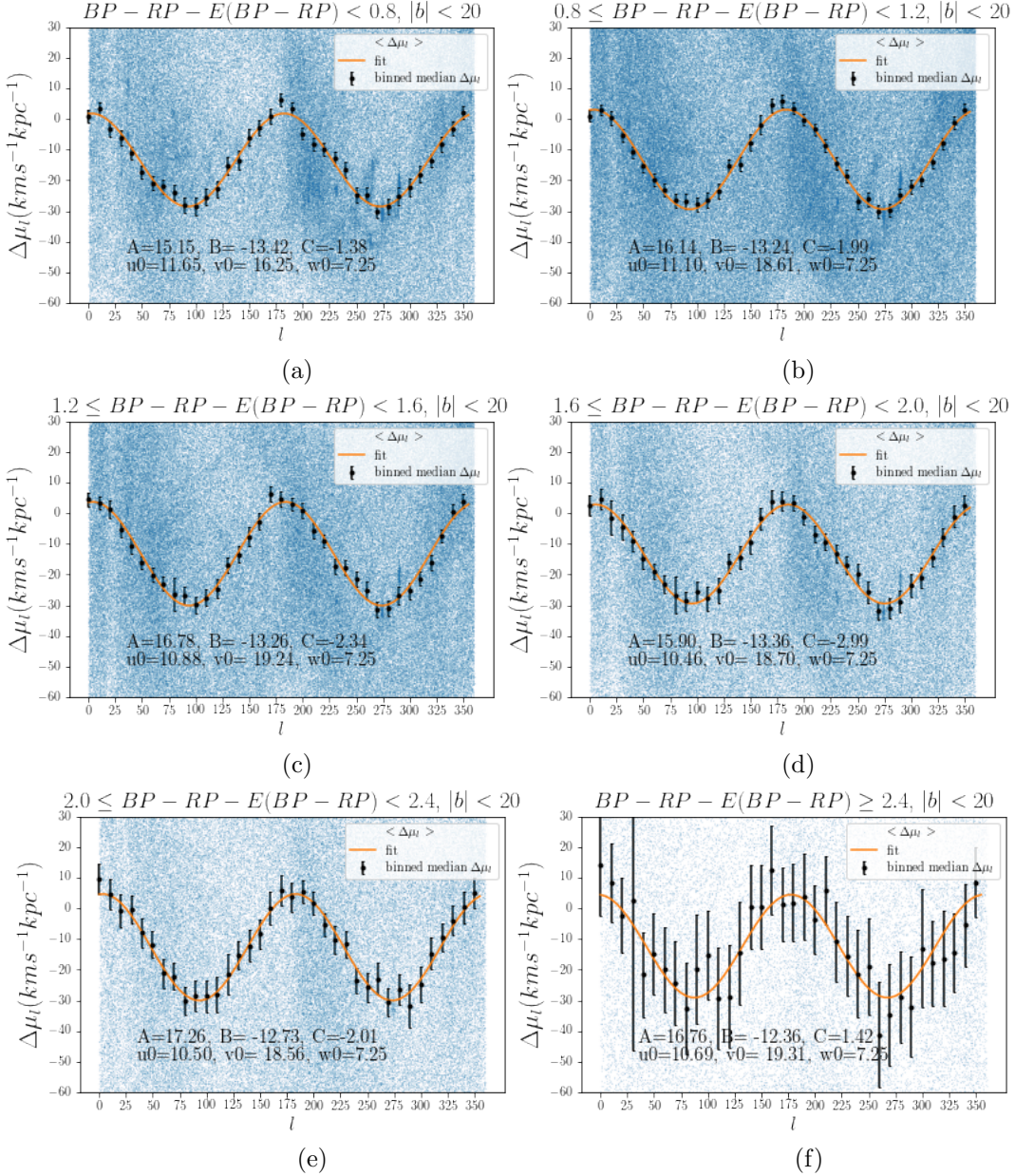


Figure 15: $\Delta\mu_l$ as a function of l for stars with $d < 500\text{pc}$ and $|b| < 20^\circ$ divided into groups with $G_{BP} - G_{RP} - E(BP - RP) < 0.8$, $0.8 \sim 1, 2$, $1.2 \sim 1, 6$, $1.6 \sim 2.0$, $2.0 \sim 2.4$ and ≥ 2.4 .

group. Fig. 18 shows the parameter MCMC fit result for the bluest $BP - RP - (E(BP - RP)) < 0.8$ stellar group.

3.3.2. Applying filtering criteria based on Simulation to Gaia DR2

In Section 3.1, we show that in the toy model simulation, by limiting the galactic distance to less than 1kpc and attitude to less than 20° , μ_l and v_{los} are good tracers for deriving the Oort constants. In Fig. 19, we expand the distance cut off on DR2

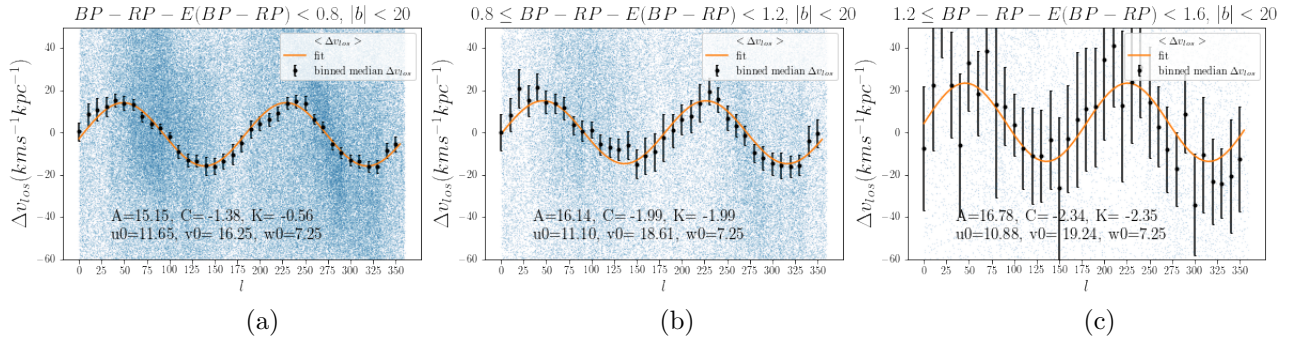


Figure 16: Δv_{los} as a function of l for stars with $d < 500\text{pc}$ and $|b| < 20^\circ$ divided into groups with $G_{BP} - G_{RP} - E(BP - RP) < 0.8$, $0.8 \sim 1.2$, $1.2 \sim 1.6$, and $1.6 \sim 2.0$.

Table 3: The values of the Oort Constants and their uncertainties estimated from the results in Fig. 15, 16 and 17 using MCMC. For the two bluest groups (top two rows), $\Delta\mu_l$, $\Delta\mu_b$ and Δv_{los} are considered together in MCMC. Only $\Delta\mu_l$ and $\Delta\mu_b$ are included for the next three color groups. And for the last population in the table, the reddest population, only μ_l is considered, thus, the value of K is not estimated.

$BP - RP - E(BP - RP)$	$A(\text{km/s/kpc})$	$B(\text{km/s/kpc})$	$C(\text{km/s/kpc})$	$K(\text{km/s/kpc})$
< 0.8	15.00 ± 0.24	-13.32 ± 0.22	-1.66 ± 0.31	-0.93 ± 0.36
≥ 0.8 and < 1.2	15.93 ± 0.31	-13.18 ± 0.24	-1.96 ± 0.26	-0.67 ± 0.43
≥ 1.2 and < 1.6	16.78 ± 0.40	-13.35 ± 0.28	-2.32 ± 0.33	-2.18 ± 1.04
≥ 1.6 and < 2.0	15.83 ± 0.44	-13.36 ± 0.38	-2.70 ± 0.46	-2.09 ± 1.09
≥ 2.0 and < 2.4	17.15 ± 0.83	-12.88 ± 0.55	-2.00 ± 0.78	-3.20 ± 1.49
≥ 2.4	17.02 ± 2.12	-12.64 ± 1.43	-0.94 ± 2.16	NA

data to 1kpc. The corresponding fitted Oort constants are: $A = 16.04 \pm 0.09$, $B = -13.62 \pm 0.07$, $C = -1.88 \pm 0.10$, $K = -1.85 \pm 0.21$ km/s/kpc. It is shown in these plots that at 1kpc, for all three motions, the deviation from the predicted double sinusoidal models are larger than those at 500 pc. This deviation possible come from including stars fruther away from the MW plane with a larger Galactic distance but the same value for Galactic latitude. Still, the fitted Oort constants are relatively in agreement with those in Table 3. This implies distance is a less strict cut-off criterion than the restriction that the Taylor expansion in Eq. 6 implies.

4. DISCUSSION

For our test particle simulations, based on the comparison of the longitudinal profiles of μ_l and v_{los} under different Glacatic distance and latitudinal restrictions in Section 3.1, we choose $d < 1\text{kpc}$ and $|b| < 20^\circ$ as the sampling criteria in extracting the longitudinal profiles of $\mu_l/\cos b$ and v_{los}/d . And we ignore $\mu_b/\cos b \sin b$ in deriving the Oort constants because its much larger deviation compared to $\mu_l/\cos b$ and v_{los}/d . With MCMC that includes only $\mu_l/\cos b$ and v_{los}/d , we determine the best-fitting

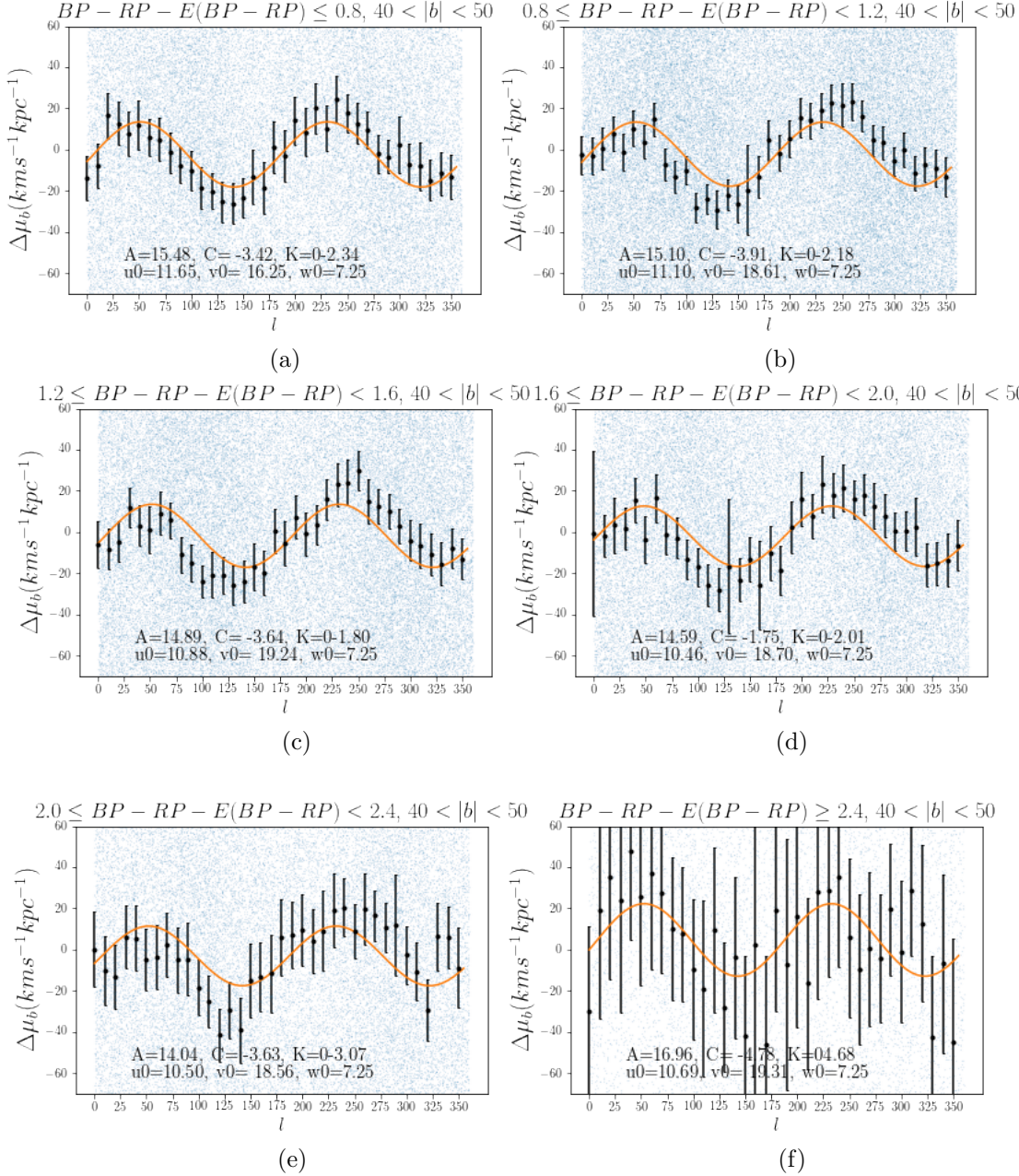


Figure 17: $\Delta\mu_b$ as a function of l for stars with $d < 500$ pc and $40^\circ < |b| < 50^\circ$ divided into groups with $G_{BP} - G_{RP} - E(BP - RP) < 0.8, 0.8 \sim 1, 2$, and $1.2 \sim 1.6$.

Oort constants and their uncertainties as: $A = 15.62 \pm 0.34, B = -12.78 \pm 0.31, C = 1.31 \pm 0.40, K = 0.24 \pm 1.09$, in the unit of km/s/kpc.

In our simulation, the theoretical slope of rotation curve under MWpotential2014 is $-(A + B) = \frac{dv_T}{dR} = -2.90$ km/s/kpc. We also know from Eq. 1 that $A - B = \frac{v_{circ\odot}}{R_\odot} = \frac{240}{8.3} = 28.92$ km/s/kpc. Therefore, the theoretical values for A and B are: $A = 15.84, B = -12.94$ km/s/kpc. The values obtained in our simulation are in good

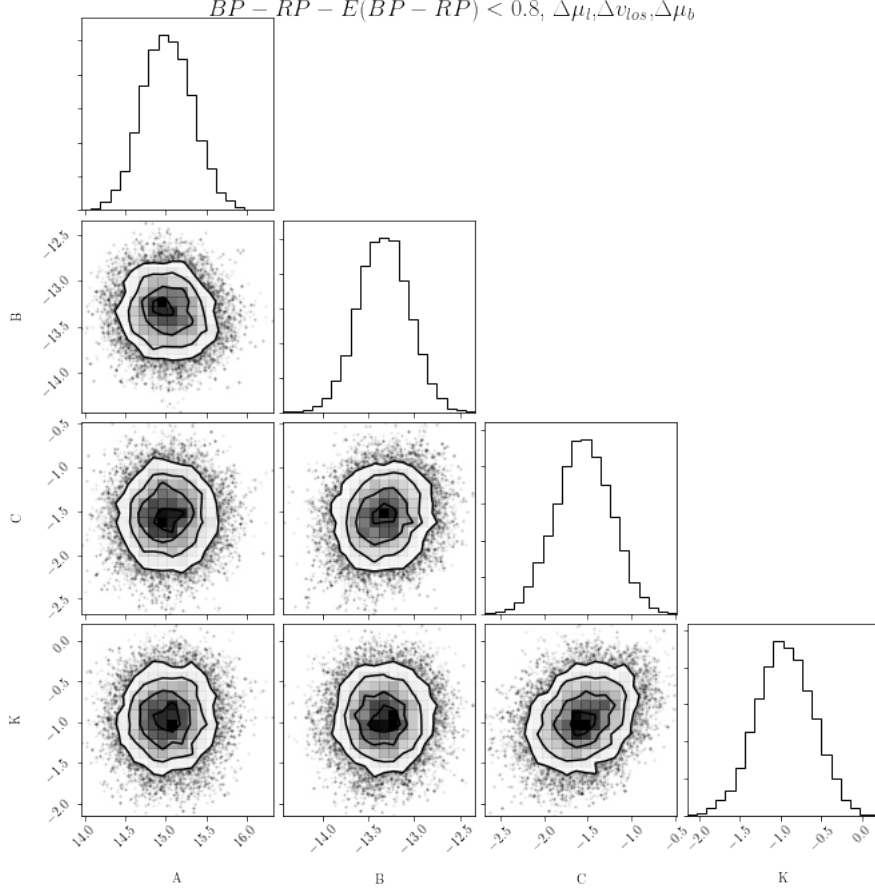


Figure 18: Fit result of the Oort constants (A, B, C, K) for $BP - RP - E(BPRP) < 0.8$ using $\Delta\mu_l$, $\Delta\mu_b$ and Δv_{los} . Similar plots have been made for all the other color groups.

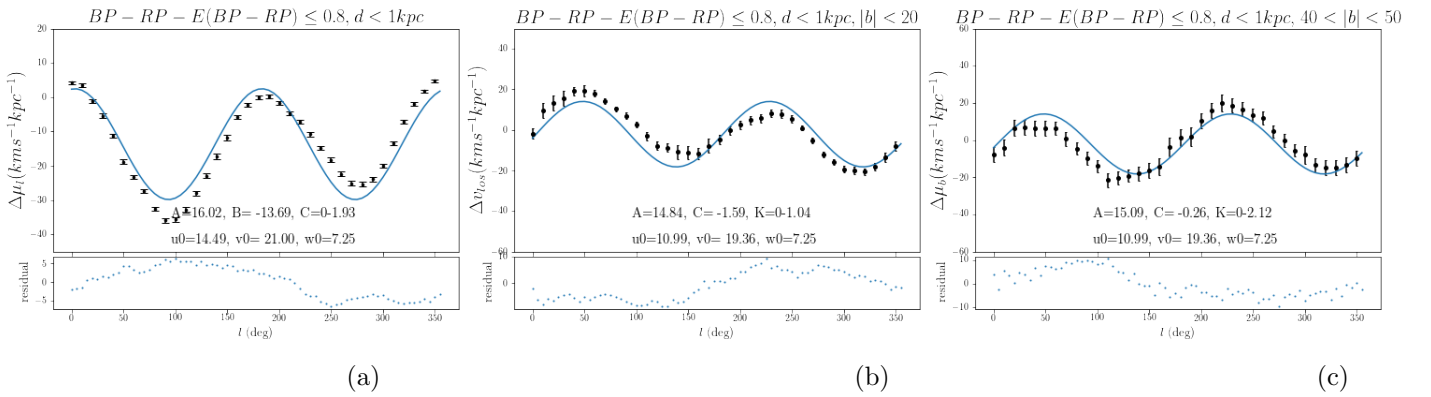


Figure 19: The longitudinal profiles of $\Delta\mu_l$, Δv_{los} and $\Delta\mu_b$ for stars with $d < 1 \text{ kpc}$ and $G_{BP} - G_{RP} - E(BP - RP) < 0.8$ in *Gaia DR2*. The scattered individual data points are not included because the sample sizes are very large.

agreement with these values. Meanwhile, the estimated value of K is 0, which is consistent with the assumption of axisymmetry in the simulation.

Meanwhile, for *Gaia* DR2 data, from Table. 3, we see that the Oort constants vary among different color groups. For the two reddest population with $BP - RP - E(BP - RP) > 2.0$, the estimated value of A and B differ significantly from the theoretical values above. The uncertainties in the parameters are also larger for these kinematically older groups with larger velocity dispersion. It also seems that the values of A and B do not have strong and consistent dependency on the stellar age.

Thus, we conclude that the $\Delta\mu_l$ and Δv_{los} of the two bluest stellar population in *Gaia* DR2 data, $BP - RP - E(BP - RP) < 1.2$, in 500pc from the Sun and latitude of less than 20° are the relatively accurate tracers to derive the Oort constants. This data filtering criteria yields:

$$A = 15.52 \pm 0.22, B = -13.33 \pm 0.17, C = -1.88 \pm 0.08, K = -1.86 \pm 0.19 \text{ km/s/kpc}. \quad (20)$$

And the estimated solar peculiar motion about LSR (10.99, 19.36, 7.25) km/s. This peculiar motion is in good measurement to the result of the $BP - RP - E(BP - Rp) < 0.8$ group in [Li et al. \(2019\)](#).

The measurements for A and B from our simulations and analysis on *Gaia* DR2 are in good agreement with each other and those obtained by [Li et al. \(2019\)](#) and [Bovy \(2017\)](#). The local gradient of the rotation curve is given by $\frac{dv_\phi}{dR} = -(A + B)$. According to our results from both simulation and *Gaia* DR2, the slope of rotation curve at R_\odot is negative. It indicates that the circular velocity decreases in the solar vicinity, which is in agreement with the rotation curve in Fig. 1.

Recall in the Introduction, we mentioned that the mean offset value K describes the divergence in the local velocity field. K from simulation is not significantly different from 0, confirming that Milky Way simulated from quasi-isothermal distribution is axisymmetric. On the other hand, the non-zero mean offset derived from *Gaia* DR2 shows the motions in our actual Milky Way is non-axisymmetric. The local radial velocity gradient is the sum of the two Oort constants C and K : $\frac{\partial v_R}{\partial R} = K + C$. The value in Eq. 20 suggest that this gradient is -3.74 ± 0.21 km/s/kpc for the DR2 observation data. Our measurement of C and K are slightly more positive than those in [Bovy \(2017\)](#) but in agreement with [Li et al. \(2019\)](#) within the corresponding uncertainties.

Our result on μ_b from simulation and *Gaia* DR2 do not agree with [Li et al. \(2019\)](#) very well. However, based on the results from our simulation, it is expected that the dispersion of μ_b and its deviation from the predicted function are larger compared to μ_l and μ_b . The comparison of the v_ϕ vs v_r phase plot between stars with $|b| < 20^\circ$ and $40^\circ < |b| < 50^\circ$ in Appendix Fig. 23 shows that the radial velocities about the GC for the stars with $40^\circ < |b| < 50^\circ$ are distributed over a larger non-zero range than the stars with $|b| < 20^\circ$. This suggests that the stars which are used to derive Oort constants from their proper motions in the latitudinal direction reside in more

non-circular orbits. Because the assumption for Oort constants is circular orbital motion, more consideration is needed when using μ_b to derive the Oort constants. In Section 3.2, we have also shown that μ_b has strong double sinusoidal dependency on l as predicted by Eq. 12 when the stars are in purely circular motions parallel to the MW mid-plane ($v_r = 0$ and $v_z = 0$).

5. CONCLUSION

The Oort constants give a predicted model for the rotation around the Sun. At the same time, they are connected to the rotation kinematics of the larger Milky Way by the rotation curve. We review and investigate the methods to derive the Oort constants from test particle simulation and *Gaia* DR2 observational data. Especially, we examine the choice on galactic latitude constraints. We find that for the idealized simulation under axisymmetric potential assumption, it is necessary to limit the distance within 1kpc and latitude range $|b| < 20^\circ$ to achieve a good fit based on the longitudinal profile of μ_l and v_{los} .

In analyzing *Gaia* DR2 observational data, the Oort constants are affected by stellar age. $\Delta\mu_l$ and Δv_{los} of the relatively bluer stars are more reliable tracers to derive the Oort constants. Although latitudinal proper motion reflects the in-plane local rotation that the Oort constants describes, in both our idealized simulations and the DR2 observation data, μ_b is not a reliable tracer to derive the Oort constants from local rotation kinematics compared to $\Delta\mu_l$ and Δv_{los} . The main reason is that stars have intrinsic vertical velocity due to vertical potential perturbation that dominate the effect we expect from the differential rotation in the MW (See Fig. 12). Constraining DR2 samples to within 500 pc from the Sun and latitude lower than 20° gives a fair approximation to the 2D solar vicinity region that the theoretical Oort constants derivation assumes. Using $\Delta\mu_l$ and Δv_{los} , we estimate the Oort constants as $A = 15.52 \pm 0.22$, $B = -13.33 \pm 0.17$, $C = -1.88 \pm 0.08$, and $K = -1.86 \pm 0.19$ km/s/kpc, and the slope of circular velocity at solar orbit is -18.26 ± 0.28 km/s/kpc.

In Appendix 6.1, we address that the lack of extinction and color excess data prevents us from using similar procedures to analyze EDR3. These data are expected to be published in DR3 in the first half of 2022 (Gaia Collaboration et al. 2020). The result from this work provides guidance for deriving the Oort constants from DR3 once these data are available.

ACKNOWLEDGMENTS

This work has made use of data from the European Space Agency (ESA) mission *Gaia* (<https://www.cosmos.esa.int/gaia>), processed by the *Gaia* Data Processing and Analysis Consortium (DPAC, <https://www.cosmos.esa.int/web/gaia/dpac/consortium>). Funding for the DPAC has been provided by national institutions, in particular the institutions participating in the *Gaia* Multilateral Agreement.

I would like to acknowledge the tremendous research opportunity offered by Dr.Zhaoyu Li and Dr.Juntai Shen from Shanghai Jiaotong University, as well as Prof. Karen Masters from Haverford College, and their continuous supports throughout this long and special year during the pandemic.

Software: Astropy (Astropy Collaboration et al. 2013, 2018), galpy (Bovy 2015), emcee (Foreman-Mackey et al. 2013) .

REFERENCES

- Astropy Collaboration, Robitaille, T. P., Tollerud, E. J., et al. 2013, A&A, 558, A33, doi: [10.1051/0004-6361/201322068](https://doi.org/10.1051/0004-6361/201322068)
- Astropy Collaboration, Price-Whelan, A. M., SipHocz, B. M., et al. 2018, aj, 156, 123, doi: [10.3847/1538-3881/aabc4f](https://doi.org/10.3847/1538-3881/aabc4f)
- Binney, J. 2010, MNRAS, 401, 2318, doi: [10.1111/j.1365-2966.2009.15845.x](https://doi.org/10.1111/j.1365-2966.2009.15845.x)
- Binney, J., & Merrifield, M. 1998, Galactic Astronomy
- Bovy, J. 2015, ApJS, 216, 29, doi: [10.1088/0067-0049/216/2/29](https://doi.org/10.1088/0067-0049/216/2/29)
- . 2017, MNRAS, 468, L63, doi: [10.1093/mnrasl/slx027](https://doi.org/10.1093/mnrasl/slx027)
- Eilers, A.-C., Hogg, D. W., Rix, H.-W., & Ness, M. K. 2019, ApJ, 871, 120, doi: [10.3847/1538-4357/aaf648](https://doi.org/10.3847/1538-4357/aaf648)
- Feast, M., & Whitelock, P. 1997, MNRAS, 291, 683, doi: [10.1093/mnras/291.4.683](https://doi.org/10.1093/mnras/291.4.683)
- Foreman-Mackey, D., Hogg, D. W., Lang, D., & Goodman, J. 2013, PASP, 125, 306, doi: [10.1086/670067](https://doi.org/10.1086/670067)
- Gaia Collaboration, Brown, A. G. A., Vallenari, A., et al. 2020, arXiv e-prints, arXiv:2012.01533. <https://arxiv.org/abs/2012.01533>
- Gaia Collaboration, Prusti, T., de Bruijne, J. H. J., et al. 2016, A&A, 595, A1, doi: [10.1051/0004-6361/201629272](https://doi.org/10.1051/0004-6361/201629272)
- Gaia Collaboration, Brown, A. G. A., Vallenari, A., et al. 2018, A&A, 616, A1, doi: [10.1051/0004-6361/201833051](https://doi.org/10.1051/0004-6361/201833051)
- Green, G. 2018, The Journal of Open Source Software, 3, 695, doi: [10.21105/joss.00695](https://doi.org/10.21105/joss.00695)
- Joy, A. H. 1939, ApJ, 89, 356, doi: [10.1086/144060](https://doi.org/10.1086/144060)
- Kerr, F. J., & Lynden-Bell, D. 1986, MNRAS, 221, 1023, doi: [10.1093/mnras/221.4.1023](https://doi.org/10.1093/mnras/221.4.1023)
- Kuijken, K., & Tremaine, S. 1994, ApJ, 421, 178, doi: [10.1086/173635](https://doi.org/10.1086/173635)
- Levine, E. S., Heiles, C., & Blitz, L. 2008, ApJ, 679, 1288, doi: [10.1086/587444](https://doi.org/10.1086/587444)
- Li, C., Zhao, G., & Yang, C. 2019, ApJ, 872, 205, doi: [10.3847/1538-4357/ab0104](https://doi.org/10.3847/1538-4357/ab0104)
- Lin, C. C., Yuan, C., & Roberts, W. W., J. 1978, A&A, 69, 181
- Luri, X., Brown, A. G. A., Sarro, L. M., et al. 2018, A&A, 616, A9, doi: [10.1051/0004-6361/201832964](https://doi.org/10.1051/0004-6361/201832964)
- Metzger, M. R., Caldwell, J. A. R., & Schechter, P. L. 1998, AJ, 115, 635, doi: [10.1086/300198](https://doi.org/10.1086/300198)
- Mignard, F. 2000, A&A, 354, 522
- Minchev, I., & Quillen, A. C. 2007, MNRAS, 377, 1163, doi: [10.1111/j.1365-2966.2007.11661.x](https://doi.org/10.1111/j.1365-2966.2007.11661.x)
- Mróz, P., Udalski, A., Skowron, D. M., et al. 2019, ApJL, 870, L10, doi: [10.3847/2041-8213/aaf73f](https://doi.org/10.3847/2041-8213/aaf73f)
- Ogrodnikoff, K. 1932, ZA, 4, 190
- Olling, R. P., & Dehnen, W. 2003, ApJ, 599, 275, doi: [10.1086/379278](https://doi.org/10.1086/379278)
- Olling, R. P., & Merrifield, M. R. 1998, MNRAS, 297, 943, doi: [10.1046/j.1365-8711.1998.01577.x](https://doi.org/10.1046/j.1365-8711.1998.01577.x)
- Oort, J. H. 1927, BAN, 3, 275
- Schönrich, R., Binney, J., & Dehnen, W. 2010, MNRAS, 403, 1829, doi: [10.1111/j.1365-2966.2010.16253.x](https://doi.org/10.1111/j.1365-2966.2010.16253.x)
- Sellwood, J. A., & Carlberg, R. G. 2014, ApJ, 785, 137, doi: [10.1088/0004-637X/785/2/137](https://doi.org/10.1088/0004-637X/785/2/137)

- Siebert, A., Famaey, B., Minchev, I.,
et al. 2011, MNRAS, 412, 2026,
doi: [10.1111/j.1365-2966.2010.18037.x](https://doi.org/10.1111/j.1365-2966.2010.18037.x)
- Sofue, Y., & Rubin, V. 2001, ARA&A,
39, 137,
doi: [10.1146/annurev.astro.39.1.137](https://doi.org/10.1146/annurev.astro.39.1.137)

- Taylor, M. B. 2005, in Astronomical
Society of the Pacific Conference Series,
Vol. 347, Astronomical Data Analysis
Software and Systems XIV, ed.
P. Shopbell, M. Britton, & R. Ebert, 29
- Vasiliev, E. 2019, MNRAS, 482, 1525,
doi: [10.1093/mnras/sty2672](https://doi.org/10.1093/mnras/sty2672)
- Wegg, C., Gerhard, O., & Bieth, M. 2019,
MNRAS, 485, 3296,
doi: [10.1093/mnras/stz572](https://doi.org/10.1093/mnras/stz572)

6. APPENDIX

6.1. EDR3

In December 2020, ESA made the third early intermediate release data of *Gaia* (EDR3). This version catalogs the positions and proper motions, and other photometric data of 1.8 billion stars, with 1.6 billions entries of which updated from DR2. EDR3 does not contain new radial velocity data. It adopted the 7.2 million data in DR2 after deleting 4000 wrong entries. We considered using the available data in EDR3 to further derive the Oort constants by the same methods for DR2. However, because EDR3 deleted several entries from DR2, including color excess and extinction (Gaia Collaboration et al. 2020), we decided not to apply our analysis to EDR3.

Extinction A_G and color excess $E(B - V)$ must be considered when making an H-R diagram to reflect the properties of stars accurately, and further grouping stars into different color populations that vary in their kinematic properties. However, spectroscopic data, such as radial velocity, extinction, and color excess are not yet available for the 100 million newly added stars in EDR3. These data are expected to be published in DR3 in the first half of 2022 (Gaia Collaboration et al. 2020).

We use the *DUSTMAP* python library to estimate $E(B - V)$ in EDR3. The reason for not doing doing a cross-match with DR2 samples is that the new spectroscopic measurements in EDR3 and DR3 use different blue and red photometers than those in DR2. *DUSTMAP* gives a 3D map of interstellar dust reddening probabilistically based on broadband photometric measurement from Pan-STARRS 1, 2MASS, and *Gaia* parallaxes (Green 2018). Each (l, b, d) corresponds to a color excess value in the default *bayestar17* module in *DUSTMAP*. Multiplying color excess by $R_v = 3.1$ gives us the corresponding extinction value. For EDR3, the Galactic coordinates (l, b, d) are first retrieved from TOPCAT, then used to find $E(B - V)$ and A_G in python script. Fig. 20 shows the H-R diagram after correcting parallax, extinction and color excess as described above. For the purpose of comparison with the H-R diagram of DR2 in Fig. 4, the scale and limits are set to the same as those in Fig. 4. The value of color excess given by *DUSTMAP* is larger compared to the actual measurement in DR2. This means it is not appropriate to use the criteria based on $BP - RP - E(BP - RP)$ in Li et al. (2019) to divide stellar samples into different color groups. Therefore, we do not analyze the data from EDR3 but leave them for research in the future.

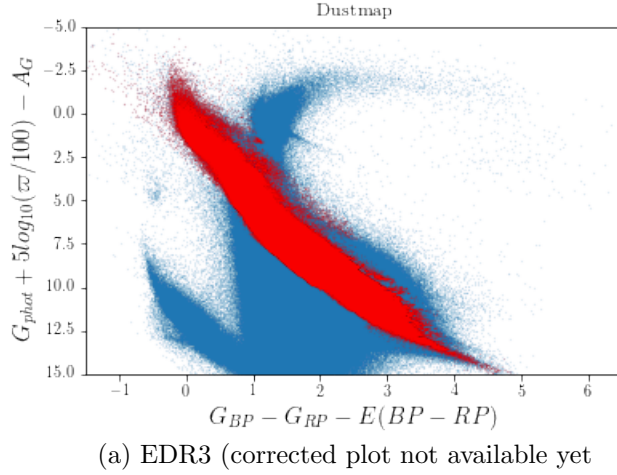


Figure 20: The H-R diagram and Main sequence star samples in EDR3 after parallax, extinction and color excess correction interpolated with DUSTMAP. For the purpose of comparison with the H-R diagram of DR2 in Fig. 4, the scale and limits are set to the same as those in Fig. 4.

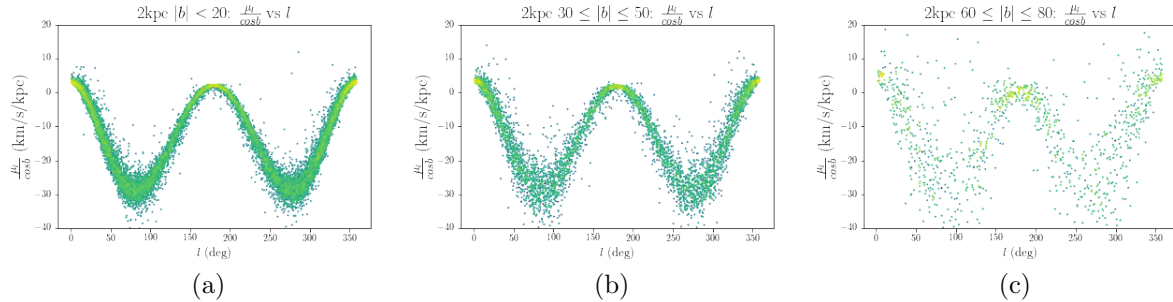


Figure 21: The distribution of $\mu_l / \cos b$ over l for stars with $d < 2\text{kpc}$ and (b) $|b| < 20^\circ$, (b) $30^\circ \leq |b| \leq 50^\circ$, and (c) $60^\circ \leq |b| < 80^\circ$.

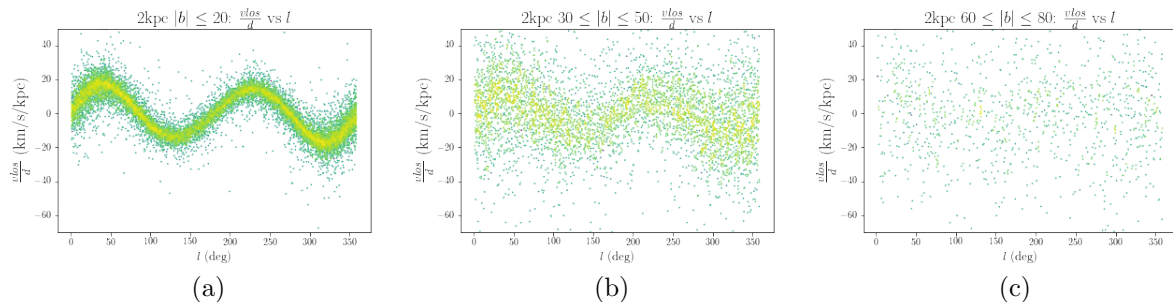


Figure 22: The distribution of v_{los} / d over l for stars with $d < 2\text{kpc}$ and (a) $|b| < 20^\circ$, (b) $30^\circ \leq |b| \leq 50^\circ$, and (c) $60^\circ \leq |b| < 80^\circ$.

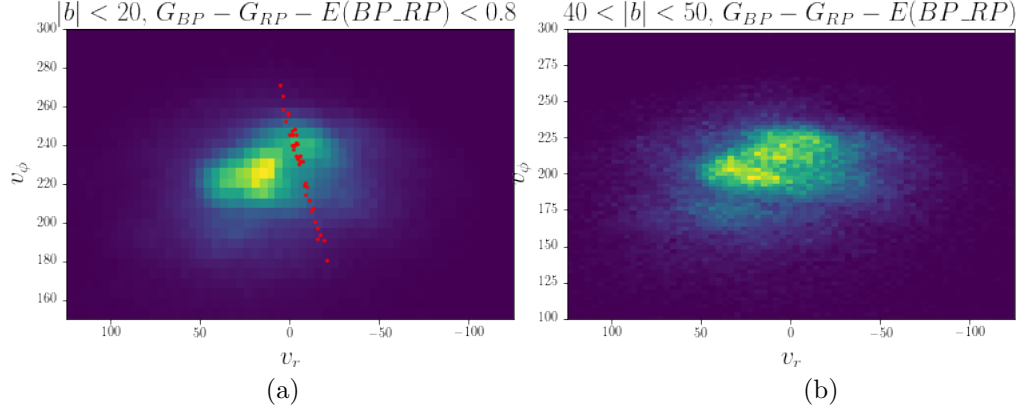


Figure 23: *Gaia* DR2: The phase plot of v_r VS v_ϕ for stars at $|b| < 20^\circ$ and $40^\circ < |b| < 50^\circ$ within 500 pc from the Sun for the stellar population with $G_{BP} - G_{RP} - E(BP_RP) < 0.8$. For $|b| < 20^\circ$, more data are centered around $v_\phi = 240$ and $v_r = 0$, which resembles circular orbit in the solar vicinity. And the red scatter points represent v_ϕ and v_r of the stars in the over dense region in Fig. 15.a.